

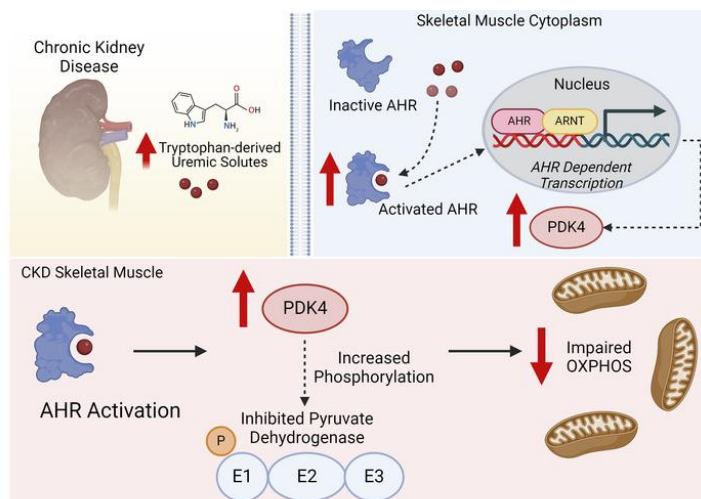
## A tryptophan-derived uremic metabolite-Ahr-Pdk4 axis governs skeletal muscle mitochondrial energetics in chronic kidney disease

Trace Thome, ... , Salvatore T. Scali, Terence E. Ryan

JCI Insight. 2024. <https://doi.org/10.1172/jci.insight.178372>.

Research In-Press Preview Muscle biology Nephrology

### Graphical abstract



Find the latest version:

<https://jci.me/178372/pdf>



1 **A tryptophan-derived uremic metabolite-Ahr-Pdk4 axis governs skeletal muscle**  
2 **mitochondrial energetics in chronic kidney disease**

3  
4  
5  
6  
7  
8  
9  
10  
11  
12  
13  
14  
15  
16  
17  
18  
19  
20  
21  
22  
23  
24  
25  
26  
27  
28  
29  
30  
31  
32  
33  
34  
35  
36  
37  
38  
39

Trace Thome<sup>1</sup>, Nicholas A. Vugman<sup>1</sup>, Lauren E. Stone<sup>1</sup>, Keon Wimberly<sup>1</sup>, Salvatore T. Scali<sup>2,5</sup>, Terence E. Ryan<sup>1,3,4,#</sup>

<sup>1</sup>Department of Applied Physiology and Kinesiology, <sup>2</sup>Division of Vascular Surgery and Endovascular Therapy, <sup>3</sup>Myology Institute, <sup>4</sup>Center for Exercise Science, University of Florida, Gainesville, FL, USA.

<sup>5</sup>Malcom Randall VA Medical Center, Gainesville, FL, USA.

#Correspondence should be addressed to Terence E. Ryan, PhD: 1864 Stadium Rd, Gainesville, FL, 32611. Tel: 352-294-1700 (office); email: [ryant@ufl.edu](mailto:ryant@ufl.edu)

Running Head: AHR activation and muscle mitochondria in CKD

**Conflict of Interest:** The authors have declared that no conflicts of interest exist.

40 **ABSTRACT**

41 Chronic kidney disease (CKD) causes an accumulation of uremic metabolites that  
42 negatively impact skeletal muscle function. Tryptophan-derived uremic metabolites are  
43 agonists of the aryl hydrocarbon receptor (AHR) which has been shown to be activated  
44 in the blood of CKD patients. This study investigated the role of the AHR in skeletal  
45 muscle pathology of CKD. Compared to control participants with normal kidney function,  
46 AHR-dependent gene expression (*CYP1A1* and *CYP1B1*) was significantly upregulated  
47 in skeletal muscle of patients with CKD ( $P=0.032$ ) and the magnitude of AHR activation  
48 was inversely correlated with mitochondrial respiration ( $P<0.001$ ). In mice with CKD,  
49 muscle mitochondrial oxidative phosphorylation (OXPHOS) was significantly impaired  
50 and strongly correlated with both the serum level of tryptophan-derived uremic  
51 metabolites and AHR activation. Muscle-specific deletion of the AHR significantly  
52 improved mitochondrial OXPHOS in male mice with the greatest uremic toxicity  
53 (CKD+probenecid) and abolished the relationship between uremic metabolites and  
54 OXPHOS. The uremic metabolite-AHR-mitochondrial axis in skeletal muscle was further  
55 confirmed using muscle-specific AHR knockdown in C57BL6J that harbour a high-affinity  
56 AHR allele, as well as ectopic viral expression of constitutively active mutant AHR in mice  
57 with normal renal function. Notably, OXPHOS changes in  $AHR^{mKO}$  mice were only present  
58 when mitochondria were fueled by carbohydrates. Further analyses revealed that AHR  
59 activation in mice led to significant increases in Pdk4 expression ( $P<0.05$ ) and  
60 phosphorylation of pyruvate dehydrogenase enzyme ( $P<0.05$ ). These findings establish  
61 a uremic metabolite-AHR-Pdk4 axis in skeletal muscle that governs mitochondrial deficits  
62 in carbohydrate oxidation during CKD.

## 63 INTRODUCTION

64 Chronic kidney disease (CKD) affects over ~500 million people globally (1). CKD  
65 results in a progressive skeletal myopathy characterized by reduced muscle mass and  
66 strength, increased fatiguability, and exercise intolerance (2-5). The imbalance between  
67 muscle catabolic and anabolic pathways have been well-documented in CKD, including  
68 the overactivation of the ubiquitin proteasome system, dysregulation of autophagy,  
69 increased caspase and calpains, and impaired insulin growth like factor 1 (IGF-1)  
70 signaling which manifests as severe muscle wasting (6-15). Recently, skeletal muscle  
71 mitochondrial and redox abnormalities have emerged as potential causal factors driving  
72 the skeletal myopathy in CKD (2, 16-28), however the mechanisms governing metabolic  
73 changes are not fully understood.

74 The accumulation of uremic metabolites and solutes is considered a hallmark of  
75 CKD and have deleterious effects to multiple tissues (29-32). Indoxyl sulfate (IS), a well-  
76 known uremic metabolite, has been shown to impair mitochondrial respiration, increase  
77 oxidative stress, and result in muscle atrophy in mice with normal kidney function (26, 27,  
78 33). Kynurenines are another class of uremic metabolites that accumulate in CKD  
79 patients and have been associated with low walking speed, grip strength, and frailty in  
80 non-CKD adults (34-36). Both indoles and kynurenines are derived from tryptophan  
81 catabolism and, interestingly, are ligands for the aryl hydrocarbon receptor (AHR) (37,  
82 38), a ubiquitously expressed ligand activated transcription factor involved in xenobiotic  
83 metabolism of both endogenous and exogenous molecules (39, 40). Chronic AHR  
84 activation, primarily studied in the context of exposure to dioxin, is toxic in the liver,  
85 reproductive organs, immune system, and central nervous system (39, 41-43). These

86 toxic effects have been associated with disruption of circadian rhythm, metabolic  
87 syndrome, and type II diabetes (42, 44, 45). Elevated levels of AHR activation have been  
88 identified in the blood of CKD patients (46) and in several tissues of rodents with CKD(47).  
89 In skeletal muscle, recent work has shown that AHR activation phenocopies the skeletal  
90 myopathy caused by tobacco smoking (48) and contributes to worsened myopathy  
91 outcomes in the context of limb ischemia (49). Based on the prior evidence, this study  
92 aimed to test whether AHR activation links the accumulation of uremic metabolites to  
93 muscle dysfunction in CKD.

94

## 95 **RESULTS**

96 ***AHR activation is present in skeletal muscle of human patients and rodents with***  
97 ***CKD.*** Several uremic metabolites that accumulate in the serum of CKD patients are  
98 derived from tryptophan catabolism (50-53) (**Figure 1A**). To explore if the accumulation  
99 of tryptophan-derived uremic metabolites results in AHR activation in skeletal muscle, we  
100 employed quantitative PCR (qPCR) to measure the mRNA expression of the *AHR* and  
101 downstream cytochrome P450 genes, *CYP1A1* and *CYP1B1*, in gastrocnemius muscle  
102 from participants with and without CKD. *AHR* and *CYP1A1* mRNA expression were  
103 increased ~11.5 and ~10.3-fold in muscle from CKD patients when compared to controls  
104 (**Figure 1B**). *CYP1B1* was increased ~6.6-fold in CKD, but this was not statistically  
105 significant ( $P=0.525$ ) (**Figure 1B**). The expression of *CYP1A1* (a surrogate for AHR  
106 activation) had a significant inverse association with muscle mitochondrial respiration  
107 rates in permeabilized myofibers (**Figure 1C**). Immunoblotting performed on the  
108 quadriceps muscle of mice confirmed the presence of the AHR protein, although

109 abundance was not impacted by CKD and was lower than the liver (**Figure 1D**). Next,  
110 cultured murine (C2C12) myotubes treated with 100 $\mu$ M of tryptophan-derived uremic  
111 metabolites (IS, kynurenic acid (KA), L-kynurenine (L-Kyn), and indole-acetic acid (IAA))  
112 displayed increases in *Cyp1a1* mRNA expression (**Figure 1E**). These data demonstrate  
113 that the AHR is expressed in human and mouse skeletal muscle and activated in the  
114 context of CKD and by tryptophan-derived uremic metabolites.

115

116 ***Uremic metabolite accumulation drives skeletal muscle AHR activation in CKD and***  
117 ***can be disrupted by muscle-specific AHR deletion.*** To determine if serum levels of  
118 uremic metabolites are responsible for AHR activation in skeletal muscle, we generated  
119 an inducible skeletal muscle-specific knockout mouse (AHR<sup>mKO</sup>). Deletion of the AHR was  
120 confirmed in skeletal muscle by DNA recombination (**Supplemental Figure 2A**) and the  
121 ablation of AHR signaling (*Cyp1a1* mRNA expression) in muscle exposed to IS  
122 (**Supplemental Figure 2B**). Next, we explored the link between uremic metabolite  
123 accumulation and AHR activation using wildtype littermates (AHR<sup>fl/fl</sup>) and AHR<sup>mKO</sup> mice  
124 fed either a casein control (Con) or adenine-supplemented diet (CKD), as well as CKD-  
125 mice treated twice daily with probenecid, an organic anion transporter inhibitor which has  
126 been shown to further increase uremic metabolite levels by preventing tubular secretion  
127 (54) (**Figure 2A**). L-Kyn, KA, and the L-Kyn to tryptophan ratio (Kyn/Tryp) were all  
128 significantly elevated in probenecid treated male mice with CKD (**Figure 2B**).  
129 Interestingly, kynurenine concentrations remained unchanged in females while KA and  
130 Kyn/Tryp were significantly elevated in both CKD only and probenecid groups (**Figure**  
131 **2C**). *Cyp1a1* and *Ahrr* (genes regulated by the AHR) were significantly increased in

132 muscle from AHR<sup>fl/fl</sup> male mice and unaffected in the AHR<sup>mKO</sup> mice (**Figure 2D**). However,  
133 females elicited lower activation of AHR dependent genes compared to males (**Figure**  
134 **2E**). These sex-dependent effects appear to be independent of the severity of CKD as  
135 both males and females displayed similar glomerular filtration rates (GFR, **Supplemental**  
136 **Figure 2C**) and blood urea nitrogen levels (**Supplemental Figure 2D**).

137

138 ***Deletion of the AHR disrupts uremia induced mitochondrial OXPHOS dysfunction***  
139 ***in skeletal muscle.*** Next, we sought to determine if the significant association between  
140 *CYP1A1* expression levels and mitochondrial respiratory function observed in skeletal  
141 muscle from patients with and without CKD (**Figure 1C**) was mediated by the AHR.  
142 Mitochondria were isolated from the muscle of AHR<sup>fl/fl</sup> and AHR<sup>mKO</sup> mice and respirometry  
143 was performed using a creatine kinase (CK) clamp to titrate the extra mitochondrial  
144 ATP/ADP ratio ( $\Delta G_{ATP}$ , a representation of cellular energy demand). The relationship  
145 between  $\Delta G_{ATP}$  and oxygen consumption ( $JO_2$ ) represents the conductance through the  
146 mitochondrial OXPHOS system (**Figure 3A**). Using a mixture of carbohydrate and fatty  
147 acid to fuel mitochondria,  $JO_2$  and OXPHOS conductance was significantly decreased in  
148 mice with CKD (**Figure 3B**). However, deletion of the AHR did not significantly improve  
149 OXPHOS in CKD mice (**Figure 3B**). When probenecid was administered to mice with  
150 CKD to increase uremic metabolite levels and AHR activation in skeletal muscle further,  
151 deletion of the AHR was found to have sex- and fuel source-dependent effects on muscle  
152 mitochondrial OXPHOS. Under these conditions, AHR<sup>mKO</sup> failed to protect females from  
153 OXPHOS impairment when mitochondria were fueled by a mixture of carbohydrates and  
154 fatty acid (**Figure 3C**), consistent with the results in CKD mice without probenecid

155 treatment. However, when mitochondria were energized with carbohydrates (pyruvate  
156 and malate), male  $AHR^{mKO}$  mice had significantly higher OXPHOS conductance  
157 compared to  $AHR^{fl/fl}$  littermates ( $P=0.045$  **Figure 3D**). No significant effect of  $AHR^{mKO}$  was  
158 observed when mitochondria were fueled only with the medium chain fatty acid  
159 octanoylcarnitine in males (**Figure 3E**) or in any condition in female mice (**Figure 3C-E**).

160 Interestingly, elevated mRNA expression of pyruvate dehydrogenase kinase 4  
161 (*Pdk4*), a negative regulator of pyruvate metabolism, was upregulated in male  $AHR^{fl/fl}$   
162 mice with CKD+probenecid but not  $AHR^{mKO}$  mice (**Supplemental Figure 3A**), which  
163 could explain the protection of OXPHOS observed in  $AHR^{mKO}$  mice when pyruvate is the  
164 primary carbon source. Mitochondrial  $H_2O_2$  production was unaffected by the presence  
165 of CKD or the deletion of the AHR in either sex (**Supplemental Figure 3B**). Additionally,  
166 probenecid treatment alone did not have an impact on OXPHOS conductance in skeletal  
167 muscle mitochondria (**Supplemental Figure 4**). We observed strong inverse correlations  
168 between uremic metabolite levels (Kyn/Trp ratio and Kyn concentration) or AHR activation  
169 (*Ahrr* expression) and OXPHOS conductance in male  $AHR^{fl/fl}$  mice, but not in females  
170 (**Figure 3F**). Interestingly, those relationships were abolished in  $AHR^{mKO}$  male mice.  
171 These findings agree with the observed relationship between AHR activation and  $JO_2$  in  
172 human CKD skeletal muscle (**Figure 1C**) and previous work in non-CKD rodents exposed  
173 to elevated kynurenines (55). While CKD decreased muscle mass, myofiber size/area,  
174 grip strength, and isometric contractile performance, deletion of the AHR did not attenuate  
175 these changes in either sex (**Supplemental Figures 5 and 6**).

176

177 **Muscle-specific knockdown of the AHR in CKD mice expressing a high-affinity AHR**  
178 **allele improves mitochondrial OXPHOS.** While the AHR is well conserved across  
179 species, naturally occurring polymorphisms in the sequence exist and confer differences  
180 in the affinity for ligands (56-58). The AHR<sup>fl/fl</sup> mice used to generate the AHR<sup>mKO</sup> mice  
181 herein were derived from 129-SvJ embryonic stem cells which harbor a low affinity AHR<sup>d</sup>  
182 allele that exhibits 10-100-fold lower sensitivity to xenobiotic ligands when compared to  
183 mice with the high-affinity AHR<sup>b</sup> found in C57BL/6J mice (56) (**Figure 4A**). Thus, we  
184 examined if knockdown of the AHR in muscle of C57BL/6J mice that harbor the high-  
185 affinity AHR allele would attenuate muscle pathology in CKD. Muscle-specific knockdown  
186 of the AHR was induced by systemic delivery of muscle-trophic adeno-associated virus  
187 (MyoAAV) (59) encoding a short hairpin RNA sequence targeting the AHR (shAHR) to  
188 mice with CKD (**Figure 4B**). Compared to CKD mice that received MyoAAV-GFP (green  
189 fluorescent protein), *Ahr*, *Cyp1a1*, and *Ahrr* mRNA levels were significantly reduced in  
190 the skeletal muscle of CKD mice that received MyoAAV-shAHR (**Figure 4C**). No  
191 differences were observed in AHR mRNA levels in the liver (**Supplemental Figure 7A**).  
192 Examination of mitochondrial function in the gastrocnemius muscle (**Figure 4D**) revealed  
193 significantly higher mitochondrial OXPHOS in male CKD mice that received MyoAAV-  
194 shAHR when mitochondria were fueled by a mixture of carbohydrate and fatty acid  
195 substrates, as well as carbohydrates only (both  $P < 0.01$ ), but not when energized with  
196 octanoylcarnitine alone (**Figure 4E,F**). Consistent with results from low-affinity AHR<sup>mKO</sup>  
197 mice, MyoAAV-shAHR had no effect on mitochondrial OXPHOS in female mice (**Figure**  
198 **4G,H**). Mitochondrial H<sub>2</sub>O<sub>2</sub> production, muscle mass, and muscle contractile function  
199 were not different between treatment groups (**Supplemental Figure 7**).

200

201 ***Skeletal muscle-specific expression of a constitutively active AHR (CAAHR) in***  
202 ***mice with normal kidney function impairs mitochondrial energetics.*** To isolate the  
203 role of AHR activation from the complex milieu of renal insufficiency, we generated a  
204 mutant AHR that displays constitutive transcriptional activity in the absence of ligands  
205 (60) (termed CAAHR herein). The CAAHR, or a GFP control, was delivered to mice with  
206 normal renal function using AAV9 and the skeletal muscle-specific promoter (human  
207 skeletal actin (HSA); ACTA1 gene) (**Figure 5A**). Constitutive AHR activation was  
208 confirmed via *Ahr*, *Cyp1a1*, and *Ahrr* mRNA expression (**Figure 5B**). Interestingly,  
209 *Cyp1a1* expression was higher in females than males treated with AAV-CAAHR, but this  
210 was not caused by sex-dependent differences in *Ahr* repression as *Ahrr* expression was  
211 similar between males and females (**Figure 5B**). Skeletal muscle OXPHOS function was  
212 significantly lower in AAV-CAAHR mice compared to AAV-GFP mice, regardless of sex  
213 (**Figure 5C,D**). Mitochondrial H<sub>2</sub>O<sub>2</sub> production was unaffected by AAV-CAAHR treatment  
214 (**Figure 5E**). To explore the mechanisms underlying OXPHOS dysfunction coincident with  
215 AHR activation, we assayed several matrix dehydrogenase enzymes. AAV-CAAHR  
216 reduced the activity of pyruvate dehydrogenase (PDH), malic enzyme (ME) and aconitase  
217 in males (**Figure 5F**). In females, AAV-CAAHR decreased the activity of PDH, alpha-  
218 ketoglutarate dehydrogenase, and fumarate hydratase, but increased glutamate  
219 dehydrogenase (GDH) activity (**Figure 5F**). Additional dehydrogenase assays that were  
220 unaffected by CAAHR are shown in **Supplemental Figure 8**. Unexpectedly, AAV-  
221 CAAHR hastened muscle fatigue in male mice (**Figure 5G**) but did not affect muscle mass  
222 or strength in either sex (**Supplemental Figure 8**).

223

224 ***Ahr* activation drives *Pdk4*-induced phosphorylation of the pyruvate**  
225 ***dehydrogenase enzyme***. As OXPHOS function was altered by AHR activation primarily  
226 when pyruvate was supplied as a fuel source, we explored if post-translational  
227 modification of the PDH enzyme could be linked to AHR activation. The activity of PDH  
228 is regulated by its phosphorylation status, where pyruvate dehydrogenase kinases  
229 (PDKs) decrease activity and pyruvate dehydrogenase phosphatases (PDPs) increase  
230 activity. qPCR for PDK and PDP genes in skeletal muscle revealed a significant increase  
231 in the mRNA expression of *Pdk4* in both male and female mice treated with AAV-CAAHR,  
232 while other PDK isoforms (*Pdk1*, *Pdk2*, *Pdk3*) were unaltered (**Figure 6A**). Male mice  
233 treated with AAV-CAAHR had increased *Pdp1* expression (**Figure 6A**), suggesting a  
234 possible compensatory response to elevated *Pdk4*. Using assay for transposase-  
235 accessible chromatin (ATAC) sequencing to explore chromatin accessibility, there were  
236 more than 10,000 differentially accessible peaks between AAV-CAAHR and AAV-GFP  
237 muscle (**Figure 6B**). Accessibility to the promoter region of *Pdk4* was noticeably different  
238 between AAV-CAAHR and AAV-GFP muscle (**Figure 6C**).

239 Next, we performed immunoblotting experiments to examine PDK4 protein  
240 abundance and the phosphorylation status of the PDH enzyme. In male and female mice  
241 treated with AAV-CAAHR, PDK4 protein abundance and phosphorylation of PDHE1 $\alpha$  at  
242 serine 300 were significantly increased compared to AAV-GFP treated mice (**Figure**  
243 **6D,E**). No changes in total PDHE1 $\alpha$  protein content were observed in either sex (**Figure**  
244 **6D,E**). Additionally, we performed experiments on non-CKD control mice (Con), mice with  
245 CKD treated with MyoAAV-GFP treated, and mice with CKD treated with MyoAAV-shAHR

246 (only male analyses are shown due to no improvements found in OXPHOS of female  
247 MyoAAV-shAHR mice, Figure 4). MyoAAV-GFP mice with CKD had elevated PDK4  
248 protein abundance and increased phosphorylation of PDHE1 $\alpha$  at serine 300 when  
249 compared to non-CKD control mice (**Figure 6F**). MyoAAV-shAHR treatment significantly  
250 decreased the abundance of both the PDK4 protein and the phosphorylation of PDHE1 $\alpha$   
251 at serine 300 (**Figure 6F**). Using cultured muscle cells, IS and L-Kyn treatment were also  
252 found to increase *Pdk4* mRNA expression and the phosphorylation of PDHE1 $\alpha$  at serine  
253 300 (**Supplemental Figure 10**). To confirm transcription regulation of *Pdk4* by the AHR,  
254 we generated a transcriptionally inept CAAHR by mutating the 39<sup>th</sup> amino acid from  
255 arginine to aspartate (R39D) which dramatically reduces DNA binding affinity (61) (**Figure**  
256 **7A**). Whereas expression of the CAAHR and R39D mutant both increase Ahr mRNA  
257 levels equally, Cyp1a1 expression was only increased in the CAAHR treated muscle cells  
258 (**Figure 7B**). *Pdk4* mRNA levels were significantly increased in muscle cells treated with  
259 the CAAHR, whereas the R39D mutant and GFP-treated muscle cells had similar *Pdk4*  
260 expression (**Figure 7C**). Compared with GFP or R39D treated muscle cells, CAAHR  
261 treated cells had significantly impaired pyruvate-supported OXPHOS (**Figure 7D**).

## 262 **DISCUSSION**

263 A progressive skeletal myopathy has been established in patients with CKD and  
264 contributes to symptoms of exercise intolerance and lower quality of life. Whereas the  
265 pathways driving muscle wasting/atrophy in CKD have been well described (10, 62), less  
266 is understood about the metabolic insufficiency observed in skeletal muscle of these  
267 patients (4, 18, 20, 63, 64). In this study, we identified AHR activation in the skeletal  
268 muscle of patients and mice with CKD. Skeletal muscle-specific deletion of the AHR in

269 mice with CKD and elevated tryptophan-derived uremic metabolites significantly  
270 improved mitochondrial OXPHOS in male mice only, and these improvements were  
271 greatest when mitochondria were fueled by pyruvate rather than fatty acids.  
272 Mechanistically, AHR activation in muscle resulted in increased PDK4 expression (mRNA  
273 and protein) and subsequent phosphorylation of the PDH enzyme causing impaired  
274 enzyme activity.

275 CKD is a multifactorial disease which complicates investigations to understand  
276 skeletal muscle pathology. Contributing factors include metabolic acidosis, chronic  
277 inflammation, overactivation of renin angiotensin signaling, oxidative stress, and retention  
278 of uremic metabolites, often described as “toxins”. The accumulation of tryptophan-  
279 derived uremic metabolites including indoxyl sulfate, indole-3-acetic acid, L-kynurenine,  
280 and kynurenic acid have been associated with disease severity and mortality rates in CKD  
281 patients (65-68). Treatment with AST-120, an orally administered spherical carbon  
282 adsorbent that lowers indoxyl sulfate levels in systemic circulation (69), was reported to  
283 improve exercise capacity and muscle mitochondrial biogenesis in mice with CKD (70).  
284 However, in a randomized controlled trial with CKD patients, AST-120 failed to  
285 significantly improve walking speed, grip strength, muscle mass, or perceived quality of  
286 life (71). This brings to question whether other uremic metabolites are contributing to  
287 muscle pathology in CKD. Kynurenines have been associated with chronic inflammation  
288 and uremic symptoms in CKD patients (66) and mice with elevated circulating kynurenine  
289 display impaired muscle OXPHOS function (55). Notably, kynurenine and kynurenic acid  
290 levels increase significantly with respect to CKD severity and are incompletely removed  
291 from the blood by hemodialysis treatment (66). Moreover, prolonged PCr recovery in

292 skeletal muscle of CKD patients (a marker of in vivo mitochondrial dysfunction) was found  
293 to associate with eGFR, occurred prior to initiation of hemodialysis, and was lowest in  
294 patients receiving hemodialysis treatment (2). Thus, the progressive accumulation of  
295 uremic metabolites, especially ones that may be poorly filtered by conventional dialysis  
296 membranes, may be significant contributors to the progressive decline of mitochondrial  
297 health observed in patients with CKD.

298         Indoles and kynurenines are known ligands of the AHR (37, 38, 72), whose  
299 prolonged activation has been associated with the development of metabolic syndrome  
300 (44, 45), disruption of circadian rhythms (73), altered glucose and lipid metabolism (45,  
301 74, 75), and mitochondrial respiratory impairments (76-78). To date, only three studies  
302 have investigated the role of the AHR in skeletal muscle (26, 48, 49), although previous  
303 studies have reported AHR activation in the blood of CKD patients (46, 79). In this study,  
304 skeletal muscle-specific AHR deletion improved mitochondrial OXPHOS function in CKD  
305 mice only in combination with probenecid treatment to further elevate uremic metabolites  
306 and AHR activation. However, it is important to note that several naturally occurring AHR  
307 polymorphisms occur in mice and the AHR<sup>mKO</sup> mice used in this study harbor a less  
308 sensitive Ahr<sup>d</sup> allele, as compared to the Ahr<sup>b1</sup> allele found in C57BL/6J mice, because  
309 they were generated using 129-SvJ embryonic stem cells (80). Thus, they have lower  
310 levels of AHR activation for a given dosage of ligand compared to the AHR allele found  
311 in C57BL/6J mice. To address this issue, we performed several experiments. First,  
312 AHR<sup>mKO</sup> and littermates with CKD were treated with probenecid, an organic anion  
313 transporter inhibitor that decreases the kidney's ability to eliminate uremic toxins (54).  
314 Probenecid was found in enhance serum uremic metabolite levels and muscle AHR

315 activation (*Cyp1a1* and *Ahrr* mRNA expression), particularly in male mice (**Figure 2**).  
316 Consequently, higher levels of AHR activation caused by treatment with probenecid  
317 revealed a significant improvement in mitochondrial OXPHOS in male mice but not female  
318 mice (**Figure 3**). Next, we performed experiments in the C57BL/6J mouse that expresses  
319 the high affinity *Ahr*<sup>b1</sup> allele by employing genetic knockdown (MyoAAV-shAHR) in CKD  
320 mice. In each of these, limiting AHR activation in CKD was found to promote  
321 improvements in mitochondrial OXPHOS with carbohydrate fuels in male but not female  
322 mice. Whether or not a progressive AHR activation occurs across increasing stages of  
323 CKD in human patients remains to be explored. However, it is intriguing that two studies  
324 in patients with CKD have reported stepwise impairment of muscle mitochondrial function  
325 with increasing CKD severity. Bittel *et al.* (81) reported that carbohydrate supported  
326 mitochondrial respiration (measured *ex vivo*) decreased with CKD severity. Similarly, *in*  
327 vivo phosphorus magnetic resonance spectroscopy analyses of muscle energetics  
328 performed by Gamboa *et al.* (82) showed a progressive increase in the time constant for  
329 phosphocreatine resynthesis (an index of lower muscle oxidative capacity) with across  
330 tertiles of eGFR. While more experimentation is necessary, these observations align with  
331 our observation that AHR activation is inversely correlated with muscle mitochondrial  
332 respiration.

333

334 While the mechanisms underlying the fact that AHR deletion and knockdown  
335 improved OXPHOS in male mice only are unknown, reports of sexual dimorphism in AHR  
336 biology have been reported. For example, differences in the response to 2,3,7,8-  
337 tetrachlorodibenzodioxin (TCDD, a potent AHR agonist) treatment have been reported in

338 the livers of male and female mice (83). Furthermore, it has been reported that the ligand  
339 activated AHR complex can physically associate with the estrogen receptor, as well as  
340 the androgen receptor and alter sex hormone signaling (84). AHR activation has also  
341 been shown to promote proteasomal degradation of the estrogen receptor through the  
342 cullin 4B ubiquitin ligase pathway (85) and alter sex hormone secretion (86). It is unknown  
343 if there are sex-dependent differences in AHR biology in human patients with CKD or  
344 regarding muscle mitochondrial function, although several studies investigating muscle  
345 energetics in patients with CKD have included both male and female patients and sex  
346 differences were not specifically described (4, 18, 82)

347

348         Enhanced mitochondrial OXPHOS function in male mice with AHR deletion or  
349 knockdown was present only when pyruvate was the primary fuel source. This was similar  
350 to a recent study exploring ischemic myopathy in the context of CKD (49). Additionally,  
351 C2C12 myotubes treated with uremic serum from rodents exhibited lower OXPHOS  
352 function in the presence of glucose, but not when fueled by fatty acids (87). Regarding  
353 potential mechanisms by which AHR may impair muscle mitochondrial OXPHOS, we  
354 found that PDH activity was significantly lower in both male and female mice that received  
355 AAV-CAAHR treatment. This is noteworthy because several studies have shown that  
356 uremic metabolites alone (25), as well as CKD (22), can impair matrix dehydrogenase  
357 activity. Protein and mRNA analysis of mouse muscle from both CKD animals and those  
358 with ectopic CAAHR expression confirmed that AHR activation resulted in significant  
359 increases in the expression of PDK4, a negative regulator of the PDH enzyme, as well as  
360 phosphorylation of the PDH enzyme (**Figure 6**). Further experimentation in cultured

361 muscle cells uncovered increased PDH phosphorylation following treatment AHR ligands  
362 IS and L-Kyn (**Supplemental Figure 10**). In support of these findings, patients with CKD  
363 have been reported to display decreased PDH activity and upregulated PDK4 expression  
364 in skeletal muscle (88). Taken together, these findings establish a uremic metabolite-Ahr-  
365 Pdk4 axis as a mechanism contributing to skeletal muscle mitochondrial OXPHOS  
366 impairment in CKD.

367

368         Incongruent with our hypothesis, deletion of the AHR in skeletal muscle did not  
369 improve muscle size or function in mice with CKD. This contrasts with our recent study  
370 on the ischemic myopathy with CKD (49). A possible explanation for lack of agreement  
371 likely stems from the hypoxic/ischemic microenvironment, especially considering that the  
372 AHR's transcriptional fidelity requires dimerization with the aryl hydrocarbon receptor  
373 nuclear translocator (ARNT), which is also known as hypoxia inducible factor 1-beta  
374 (HIF1b). The lack of improvement in muscle function or size with AHR deletion observed  
375 herein may be attributed to non-AHR dependent effects of CKD and uremic metabolites.  
376 For example, indoxyl sulfate was found to increase reactive oxygen species (ROS)  
377 production via activation of NADPH oxidases in cultured muscle cells (26). This increase  
378 in NADPH oxidase activity might initiate ROS-dependent atrophy pathways (89, 90) which  
379 are elevated in CKD muscle. Other contributing factors may include metabolic acidosis,  
380 chronic inflammation, overactivation of renin angiotensin signaling in the CKD condition  
381 which do not involve the AHR.

382

383           The current study is not without limitations. First, due to limited specimen size in  
384 muscle biopsy tissue from human participants, it was not possible to perform  
385 comprehensive assessments on skeletal muscle mitochondrial function as done in the  
386 animal models. Second, although mice used were fully mature and females were  
387 ovariectomized to better mimic the post-menopausal state of most female CKD patients  
388 (91), the mice used in this study were relatively young despite age being a significant risk  
389 factor for CKD. Because the OXPHOS assessments employed require harvesting muscle  
390 tissue, these analyses were terminal and repeated temporal assessments of  
391 mitochondrial OXPHOS were not possible. Thus, we could not establish whether the  
392 mitochondrial OXPHOS impairment (secondary to AHR activation) leads to muscle  
393 atrophy or contractile dysfunction with longer durations of AHR activation. All experiments  
394 involving rodents with CKD were performed on mice fed an adenine-supplemented diet,  
395 whereas other studies have employed surgical models of CKD (5/6 nephrectomy) (92,  
396 93). We have shown that adenine and 5/6 nephrectomy models have similar levels of  
397 uremic metabolites, muscle atrophy, and mitochondrial dysfunction (24). Regarding  
398 uremic metabolites, it is worth noting that there may be differences in the relative  
399 abundance of AHR ligands in the adenine model compared to patients with CKD,  
400 although larger and more comprehensive quantification is necessary to fully assess these  
401 differences. Additionally, our metabolite analysis herein did not include quantification of  
402 indoles although we have previously reported their increase in mice fed adenine diet to  
403 induce CKD (22, 24). Probenecid, a drug that reduces uric acid levels and is used to treat  
404 gout, was employed to elevate uremic metabolites levels as done previously (54) with the  
405 goal of increasing muscle AHR activation. Adenine is a purine base that can be converted

406 to uric acid by xanthine oxidase and the combination of adenine feeding and probenecid  
407 could impact the degree of renal impairment in our experiments, although blood urea  
408 nitrogen levels were similar in CKD and CKD+probenecid mice (**Supplemental Figure**  
409 **2**). The degree of kidney injury with adenine feeding may be related to uric acid levels as  
410 inhibition of xanthine oxidase attenuated kidney injury in this model (94). Nonetheless, it  
411 is important to consider any potential effects this combination could have because  
412 hyperuricemia occurs in patients with CKD and associates with mortality (95) and uric  
413 acid release occurs in atrophying muscle (96).

414

415 Collectively, the findings herein establish a tryptophan-derived uremic metabolite-  
416 AHR-Pdk4 axis as a critical regulator skeletal muscle mitochondrial function in CKD, when  
417 fueled by pyruvate, and provide evidence that interventions that disrupt this axis can  
418 improve muscle mitochondrial function.

419

## 420 **METHODS**

421

422 **Sex as a Biological Variable.** Our study examined male and female animals, and sex-  
423 dimorphic effects are reported. Human participants included both male and female  
424 individuals (self-identified), but the sample size was not powered to detect differences in  
425 sex.

426

427 **Humans Subjects.** Muscle specimens of the gastrocnemius were collected from adult  
428 control participants with normal kidney function and patients with CKD via percutaneous

429 muscle biopsy using sterile procedures (49, 97). The physical and clinical characteristics  
430 of these participants are shown in **Supplemental Table 1**. All participants in this study  
431 were free from peripheral vascular disease and distinct from our prior study on the role of  
432 the AHR in peripheral artery disease (49). Non-CKD adult controls and patients with CKD  
433 were recruited from the UF Health Shand's hospital or Malcom Randall VA Medical  
434 Center. Inclusion criteria for CKD patients included an eGFR between 15-45  
435 mL/min/1.73\*m<sup>2</sup> for at least 3 months that were not on hemodialysis. Inclusion criteria for  
436 Non-CKD adult controls was an eGFR greater than 80 mL/min/1.73\*m<sup>2</sup>. eGFR was  
437 calculated using the CKD-EPI Creatine equation (2021) (98). Exclusion criteria for both  
438 groups included being an active smoker (must be tobacco free for >6 months) due to  
439 tobacco smoke containing AHR ligands (99). A portion of the muscle samples was  
440 cleaned and quickly snap froze in liquid nitrogen. Another portion was immediately placed  
441 in ice-cold buffer X (50 mM K-MES, 7.23 mM K<sub>2</sub>EGTA, 2.77 mM CaK<sub>2</sub>EGTA, 20 mM  
442 imidazole, 20 mM taurine, 5.7 mM ATP, 14.3 mM phosphocreatine, and 6.56 mM MgCl<sub>2</sub>-  
443 6H<sub>2</sub>O, pH 7.1) for preparation of permeabilized fiber bundles (97, 100). Fiber bundles  
444 were mechanically separated using needle-tipped forceps under a dissecting scope and  
445 subsequently permeabilized with saponin (30 µg/ml) for 30 minutes at 4°C on a nutating  
446 mixer, and then washed in ice-cold buffer Z (105 mM K-MES, 30 mM KCl, 1 mM EGTA,  
447 10 mM K<sub>2</sub>HPO<sub>4</sub>, 5 mM MgCl<sub>2</sub>-6H<sub>2</sub>O, 0.5 mg/ml bovine serum albumin (BSA), pH 7.1) for  
448 15 minutes until analysis. High-resolution O<sub>2</sub> consumption measurements were  
449 conducted at 37°C in buffer Z (in mmol/l) (105 K-MES, 30 KCl, 1 EGTA, 10 K<sub>2</sub>HPO<sub>4</sub>, 5  
450 MgCl<sub>2</sub>6H<sub>2</sub>O, 0.5 mg/ml BSA, pH 7.1), supplemented with creatine monohydrate (5 mM),  
451 using the Oroboros O2K Oxygraph. Mitochondrial respiration was measured energizing

452 the bundles with 5mM pyruvate and 2.5mM malate followed by the addition of 4mM  
453 adenosine diphosphate (ADP) to stimulate maximal respiration. At the end of  
454 experiments, the bundles were retrieved, washed in distilled water, lyophilized  
455 (Labconco), and the dry weight was obtained using a Mettler Toledo MX5 microbalance.  
456 Rates of O<sub>2</sub> consumption ( $JO_2$ ) were normalized to the bundle dry weight. All study  
457 procedures were carried out according to the Declaration of Helsinki and participants  
458 were fully informed about the research and informed consent was obtained.

459

460 **Animals.** AHR conditional knockout mice (AHR<sup>ckO</sup>) with loxP sites flanking exon 2 of the  
461 AHR (AHR<sup>tm3.1Bra/J</sup>) were obtained from Jackson Laboratory (Stock #006203). AHR<sup>ckO</sup>  
462 mice were bred with a tamoxifen inducible skeletal muscle-specific Cre line (Tg(ACTA1-  
463 cre/Esr1\*)2Kesr/J, Jackson Laboratories, Stock No. 025750) to generate skeletal muscle-  
464 specific inducible AHR knockout mice (AHR<sup>mkO</sup>). Female mice underwent bilateral  
465 ovariectomy (OVX) 14-days prior to inducing Cre-mediated DNA recombination. Deletion  
466 of the AHR was initiated at 5-months of age by intraperitoneal (IP) injection of tamoxifen  
467 (MilliporeSigma Cat. No. T5648) for five consecutive days (120mg/kg). Littermate AHR  
468 floxed mice without the Cre transgene (AHR<sup>fl/fl</sup>) that received the same tamoxifen dosing  
469 were used as controls. For adeno associated virus (AAV) experiments, C57BL/6J mice  
470 (Stock #000664) were obtained from The Jackson Laboratory at 5 months of age (N=60  
471 total mice). Female mice underwent OVX 14-days prior to delivery of AAV. All rodents  
472 were housed in a temperature (22°C) and light controlled (12-hour light/12-hour dark)  
473 room and maintained on standard chow diet (Envigo Teklad Global 18% Protein Rodent  
474 Diet 2918 irradiated pellet) with free access to food and water. All animal experiments

475 adhered to the *Guide for the Care and Use of Laboratory Animals* from the Institute for  
476 Laboratory Animal Research, National Research Council, Washington, D.C., National  
477 Academy Press.

478

479 ***Plasmid Construction and Adeno-Associated Virus Production/Delivery.*** AAV  
480 backbones were obtained from Cell Biolabs, USA (Cat. No. VPK-411-DJ). To accomplish  
481 muscle specific expression of transgenes, a human skeletal actin (*Acta1*; abbreviated as  
482 HSA) was PCR amplified from human genomic DNA from a patient's muscle biopsy. The  
483 AAV-HSA-GFP plasmid was developed by inserting the HSA promoter and GFP  
484 (ZsGreen1) into a promoter-less AAV vector (Cat. No. VPK-411-DJ; Cell BioLabs, USA)  
485 using In-Fusion Cloning (Takara Bio, USA; Cat. No. 638911). To generate a constitutively  
486 active AHR (CAAHR) vector, the mouse AHR coding sequence was PCR amplified from  
487 genomic DNA obtained from a C57BL6J mouse such that the ligand binding domain  
488 (amino acids 277–418) was deleted for the murine AHR and subsequently cloned and  
489 inserted downstream of the HSA promoter using In-Fusion cloning. The resulting  
490 plasmids were packaged using AAV2/9 serotype by Vector Biolabs (Malvern, PA). The  
491 skeletal muscle-specific AAV9's were delivered via several small volume intramuscular  
492 injections of the hindlimb muscle TA, EDL, and gastrocnemius plantar flexor complex at  
493 a dosage of  $5E+11$  vg/limb. To knockdown the AHR in skeletal muscle, we utilized an  
494 siRNA sequence (AHR siRNA: 5'-AAG UCG GUC UCU AUG CCG CTT-3') and a GFP  
495 control that were packaged using a mutated AAV9 capsid variant that enables muscle  
496 specific expression (MyoAAV4a) (101) by Vector Biolabs (Malvern, PA). MyoAAV's were  
497 delivered via a tail injection at a dosage of  $1E+11$  vg/kg. To generate a transcriptionally

498 deficient CAAHR mutant, we performed Q5 site-directed mutagenesis (NEB, Cat. No.  
499 E0554S) to mutant arginine-39 to aspartate (R39D) (61).

500

501 **RNA Isolation and quantitative PCR.** Total RNA was isolated using TRIzol (Invitrogen,  
502 Cat. No. 15-596-018). All samples were homogenized using a PowerLyzer 24 (Qiagen)  
503 and RNA was isolated using Direct-zol RNA MiniPrep kit (Zymo Research, Cat. No.  
504 R2052). cDNA was generated from 500ng of RNA using the LunaScript RT Supermix kit  
505 (New England Biolabs, Cat. No. E3010L). Real-time PCR (RT-PCR) was performed on a  
506 Quantstudio 3 (ThermoFisher Scientific) using either Luna Universal qPCR master mix  
507 for Sybr Green primers (New England Biolabs, Cat. No. M3003X) or Taqman Fast  
508 Advanced Master mix (ThermoFisher Scientific, Cat. No. 4444557). All primers and  
509 Taqman probes used in this work are listed in **Supplemental Table 2**. Relative gene  
510 expression was calculated as  $2^{-\Delta\Delta CT}$  from the control group.

511

512 **Muscle Cell Culture Experiments.** C2C12 murine myoblasts were obtained from ATCC  
513 (Cat. No. CRL-1772) and grown in Dulbecco's modified Eagle's medium (DMEM, GIBCO;  
514 Cat. No. 10569) supplemented with 10% fetal bovine serum (VWR; Cat. No. 97068) and  
515 1% penicillin streptomycin (GIBCO; Cat. No. 15140) at 37°C and 5% CO<sub>2</sub>. All cell culture  
516 experiments were performed with low passage cells (passages one through five) and in  
517 at least three biologically independent lots of myoblasts. When assessing AHR activation  
518 in muscle cells, C2C12 myoblast were incubated for 6-hours with 100µM of AHR agonist  
519 indoxyl sulfate (IS), L-kyurenine (L-Kyn), kynurenic acid (KA), and indole-3-acetic acid

520 (IAA). Myoblast were washed with phosphate buffered saline (PBS) and collected in  
521 TRIzol reagent for total RNA isolation.

522

523 **Western Blotting.** C2C12 muscle cells and snap frozen mouse tissue were homogenized  
524 in CelLytic M lysis buffer (MilliporeSigma, Cat. No. C2978) supplemented with protease  
525 and phosphatase inhibitors (ThermoScientific, Cat. No. A32961) in glass Teflon  
526 homogenizers and centrifuged at 10,000g for 10-minutes at 4°C. The supernatant was  
527 collected, and protein quantification was performed using a bicinchoninic acid protein  
528 assay (ThermoFisher Scientific; Cat. No. SL256970). 2x Laemmli buffer (BioRad; Cat.  
529 No. 161-0737) and  $\beta$ -mercaptoethanol (ACROS; Cat. No. 60-24-2) were added to the  
530 samples which were incubated in boiling water for five minutes. 10 $\mu$ l of a pre-stained  
531 ladder (BioRad; Cat. No. 1610394) was loaded in the first lane of a 7.5% Criterion TGX  
532 Stain-Free Protein Gel (BioRad; Cat. No. 5678023) while 20 $\mu$ g (cell lysate) and 100 $\mu$ g  
533 (tissue lysate) of each sample was loaded. Gel electrophoresis was run at 100V for 1.5  
534 hours and then imaged for total protein on a BioRad imager (GelDoc EZ Imager), before  
535 transferring to a polyvinylidene fluoride (PVDF) membrane using a BioRad Trans Blot  
536 Turbo system. The PVDF membrane was then imaged for total protein and incubated in  
537 blocking buffer (Licor; Cat. No. 927-60001) for one-hour at room temperature while  
538 rocking. The membrane was incubated overnight at 4°C with AHR primary antibody (NSJ  
539 Bioreagents; Cat. No. R30877, 1 $\mu$ g/ml), PhosphoDetect Anti-PDH-E1 $\alpha$  (pSer<sup>300</sup>) primary  
540 antibody (Millipore-Sigma; Cat. No. AP1064, 0.2 $\mu$ g/ml), or PDK4 primary antibody  
541 (ProteinTech; Cat. No. 12949-1-AP, 1:1000) in blocking buffer. After overnight incubation,  
542 the membranes were washed 3x10 minutes with TBS+0.01% tween. The membranes

543 were then incubated for two-hours in blocking solution with secondary antibody (Licor;  
544 Cat. No. C80118-05, 1:10,000 dilution) to detect the AHR, PDH-E1 $\alpha$  (pSer<sup>300</sup>), and PDK4,  
545 while the total PDHE1 $\alpha$  antibody was conjugated to AlexaFluor790 (Santa Cruz; Cat. No.  
546 377092AF790). Next, the membranes were then washed 3x10 minutes in TBS+0.01%  
547 tween and imaged on a Licor Odyssey CLx. Uncropped blots and gel images are provided  
548 in the Supplement.

549

550 **RNA Validation of Skeletal Muscle Specific Knockout of the AHR.** The soleus muscle  
551 was dissected from healthy AHR<sup>fl/fl</sup> mice and AHR<sup>mkO</sup> mice and incubated in Krebs buffer  
552 supplemented with 10mM glucose and gassed with 95% O<sub>2</sub> and 5% CO<sub>2</sub> at 37°C. The  
553 muscles were treated with 500 $\mu$ M indoxyl sulfate (IS) or equal volume of DMSO for 3.5  
554 hours and then processed for qPCR analysis.

555

556 **Induction of Chronic Kidney Disease (CKD).** Two weeks after tamoxifen treatment,  
557 mice were assigned to a casein-based chow diet for seven days, followed by induction of  
558 CKD via the addition of 0.2% (w/w) adenine to the diet. CKD mice were kept on 0.2%  
559 adenine diet for the duration of the study. Control mice were fed a casein-based chow  
560 diet for the entirety of the experiment.

561

562 **Delivery of Probenecid.** Mice were administered IP injections of 25mg/kg of probenecid  
563 twice daily (Invitrogen; Cat. No. P36400) or PBS (vehicle control) starting two weeks post-  
564 CKD induction, for the duration of two weeks. On the last day of injections, probenecid or

565 PBS was administered two hours prior to euthanasia. Plasma was isolated and stored at  
566 -80°C for further metabolomic analyses described below.

567

568 **Targeted Metabolomics in Mouse Plasma.** Targeted metabolomic analyses were  
569 performed by the Southeast Center for Integrated Metabolomics at the University of  
570 Florida. Under ketamine (100mg/kg) and xylazine (10mg/kg) anesthesia, blood was  
571 collected via cardiac puncture using a heparin coated syringe, centrifuged at 4,000rpm  
572 for 10 minutes, and plasma was stored at -80°C until analysis. Plasma was processed as  
573 done previously (22, 24).

574

575 **Assessment of Renal Function.** GFR was evaluated by measuring FITC-labeled inulin  
576 clearance (102, 103). GFR was assessed via blood collection from a small ~1mm tail snip  
577 at multiple time points (3, 5, 7, 10, 15, 35, 56, 75 minutes) following retro-orbital injection  
578 of FITC-labeled inulin (MilliporeSigma; Cat. No. F3272) in heparin coated capillary tubes.  
579 Blood collected was centrifuged at 4,000rpm for 10-minutes at 4°C and plasma was  
580 diluted (1:20) and loaded into a 96-well plate along with a FITC-inulin standard curve and  
581 fluorescence was detected using a BioTek Synergy II plate reader. GFR was calculated  
582 using a two-phase exponential decay. BUN was assessed from plasma collected prior to  
583 euthanasia using a commercial kit (Arbor Assays; Cat. No. K024).

584

585 **Assessment of Forelimb Grip Strength.** Bilateral forelimb grip strength was assessed  
586 using a grip strength meter (BIOSEB; Model No. BIO-GS3). Mice were encouraged to  
587 firmly grip the metal T-bar and were pulled backward horizontally with increasing force

588 until they released the T-bar. Three trials were performed allowing the mice 30-seconds  
589 to rest between each trial and the highest force was analyzed.

590

591 ***Peroneal Nerve Stimulated EDL Force Frequency and Fatigue Analysis.*** Mice were  
592 anesthetized with an IP injection of xylazine (10mg/kg) and ketamine (100mg/kg) and the  
593 distal portion of the extensor digitorum longus (EDL) tendon was sutured with a double  
594 square knot using 4-0 silk suture and the tendon was carefully cut distal to the suture.  
595 The mouse was placed prone on a thermoregulated platform (37°C) and the knee was  
596 immobilized/stabilized with a pin attached to the platform. The suture attached to the distal  
597 end of the EDL tendon was secured to a force length transducer (Cambridge Technology;  
598 Model: 2250), and two Chalgren electrodes (Cat. No. 111-725-24TP) were placed on both  
599 sides of the peroneal nerve and connected to an Aurora Scientific stimulator (701A  
600 stimulator). Data was collected using the DMC program (version v5.500, Aurora  
601 Scientific). Optimal length was determined by recording force production of twitch  
602 contractions while incrementally increasing muscle length with 60 seconds of rest  
603 between each contraction. Once optimal length was achieved, the EDL underwent a force  
604 frequency assessment by stimulating the peroneal nerve at 1, 25, 50, 75, 100, 125, 150,  
605 and 175 Hz (spaced one minute apart) using 2.4 mAmp stimulation, 0.1 ms pulse width,  
606 and a train duration of 0.5 s. Specific force was calculated by normalizing absolute force  
607 production to the EDL mass. Following force frequency analysis, the EDL was rested for  
608 two minutes, before undergoing a series of 80 contractions at 50 Hz (2.4mAmp  
609 stimulation, 0.1 ms pulse width, and train duration of 0.5 s) performed every two seconds  
610 to assess fatiguability of the muscle.

611

612 ***Mitochondrial Isolation.*** Skeletal muscle mitochondria were isolated from the  
613 gastrocnemius and quadriceps muscles. Dissected muscles were immediately placed in  
614 ice-cold Buffer A (phosphate buffered saline supplemented with EDTA (10mM), pH=7.4),  
615 and trimmed to remove connective tissue and fat before it was minced and subjected to  
616 a five-minute incubation on ice in Buffer A supplemented with 0.025% trypsin (Millipore  
617 Sigma; Cat. No. T4799). Following trypsin digestion, skeletal muscle was centrifuged at  
618 500g for five minutes and the supernatant was aspirated to remove trypsin. Digested  
619 muscle tissue was resuspended in Buffer C (MOPS (50mM), KCl (100mM), EGTA (1mM),  
620 MgSO<sub>4</sub> (5mM), bovine serum albumin (BSA; 2g/L); pH=7.1) and homogenized via a  
621 glass-Teflon homogenizer (Wheaton) for ~five-passes and subsequently centrifuged at  
622 800g for 10 minutes. The resulting supernatant was collected in a separate tube and  
623 centrifuged at 10,000g for 10-minutes to pellet mitochondria. All steps were performed at  
624 4°C. The mitochondrial pellet was gently washed with Buffer B (MOPS (50mM), KCl  
625 (100mM), EGTA (1mM), MgSO<sub>4</sub> (5mM); pH=7.1) to remove damaged mitochondria on  
626 the exterior of the pellet and then re-suspended in Buffer B. Protein concentration was  
627 determined using a bicinchoninic acid protein assay (ThermoFisher Scientific; Cat. No.  
628 A53225).

629

630 ***Skeletal Muscle Mitochondrial OXPHOS Function.*** High resolution respirometry was  
631 measured using Oroboros Oxygraph-2k (O2K) measuring oxygen consumption ( $JO_2$ ) at  
632 37°C in Buffer D (105mM K-MES, 30mM KCl, 1mM EGTA, 10mM K<sub>2</sub>HPO<sub>4</sub>, 5mM MgCl<sub>2</sub>-  
633 6H<sub>2</sub>O, 2.5mg/ml BSA, pH 7.2) supplemented with 5mM creatine (Cr). A creatine kinase

634 (CK) clamp was employed to leverage the enzymatic activity of CK, which couples the  
635 interconversion of ATP and ADP to that of phosphocreatine (PCr) and free Cr, to titrate  
636 the extra mitochondrial ATP/ADP ratio, thus the free energy of ATP hydrolysis ( $\Delta G_{ATP}$ )  
637 could be calculated(104). This approach allows assessment of mitochondrial flux across  
638 a range of physiological relevant energetic demands ( $\Delta G_{ATP}$ , heavy exercise to rest)  
639 which are controlled by altering the PCr/Cr ratio. The  $\Delta G_{ATP}$  can be plotted against the  
640 corresponding  $J_{O_2}$  creating a linear force-flow relationship, where the slope represents  
641 the conductance through the OXPHOS system. 25 $\mu$ g of mitochondria were added to the  
642 Oxygraph chamber in two milliliters of Buffer D supplemented with ATP (5mM), Cr (5mM),  
643 PCr (1mM), and CK (20U/mL) at 37°C. Conductance measurements were performed  
644 using various combinations the following substrates: pyruvate (5mM), malate (2.5mM),  
645 and octanoyl-L-carnitine (0.2mM). In all experiments, exogenous cytochrome c was  
646 added to confirm the outer mitochondrial membrane was intact.

647

648 ***JNAD(P)H Matrix Dehydrogenase Assays.*** Matrix dehydrogenase function was  
649 assessed utilizing the autofluorescence of NADH or NADPH (Ex/Em = 340/450) in a 96-  
650 well plate using a kinetic protocol on a BioTek synergy 2 multimode Microplate Reader.  
651 For all assays, Buffer D was supplemented with alamethicin (0.03 mg/mL), rotenone  
652 (0.005 mM), NAD<sup>+</sup> or NADP<sup>+</sup> (2 mM). Dehydrogenase enzymes such as pyruvate  
653 dehydrogenase (PDH) and alpha ketoglutarate dehydrogenase (AKGDH) required  
654 supplementation of cofactors Coenzyme A (0.1 mM), and thiamine pyrophosphate (0.3  
655 mM, TPP). Pre-warmed Buffer D (37°C) was loaded in a 96-well plate followed by the  
656 addition of mitochondria. Dehydrogenase activity was initiated with the addition of

657 enzyme-specific fuel sources: pyruvate (5mM, PDH), glutamate (10mM, glutamate  
658 dehydrogenase (GDH)), malate (5mM, malate dehydrogenase (MDH) and malic enzyme  
659 (ME)), alpha ketoglutarate (10 mM, AKGDH), citrate (6 mM, aconitase), fumarate (10 mM,  
660 fumarate hydratase (FH)), hydroxybutyrate (10 mM, beta hydroxy butyrate  
661 dehydrogenase ( $\beta$ HBDH)), or isocitrate (5 mM, isocitrate dehydrogenase 2 and 3  
662 (ICDH2/3)). Rates of NADH/NADPH production was calculated as a slope of linear  
663 portions of NADH/NADPH curves and converted to pmols of NADH/NADPH by a standard  
664 curve.

665

666 **Complex V Activity (ATP Synthase).** Mitochondria were lysed in Cell Lytic M and  
667 enzyme activity was measured in Buffer E (2.5mM MgCl<sub>2</sub>-6H<sub>2</sub>O, 20mM HEPES, 100mM  
668 KCl, 2.5mM KH<sub>2</sub>PO<sub>4</sub>, 1% glycerol, pH=8.0) supplemented with lactate dehydrogenase  
669 (10mM), pyruvate kinase (10mM), rotenone (0.005mM), phospho-enol-pyruvate (PEP,  
670 5mM), and NADH (0.2mM). In this assay, the ATP synthase works in reverse (hydrolysis  
671 of ATP) as the mitochondrial membrane potential was dissipated by lysis. Using a  
672 pyruvate kinase/lactate dehydrogenase coupled assay, ATP hydrolysis (by the ATP  
673 synthase) is coupled to NADH consumption in a 1:1 stoichiometry. The rate of decay of  
674 NADH autofluorescence (Ex/Em = 340/450 nm) represents ATP synthase activity.  
675 Fluorescence values were converted to pmols of NADH by a standard curve.

676

677 **Immunofluorescence Microscopy.** 10 $\mu$ m-thick transverse sections were cut from the  
678 tibialis anterior, extensor digitorum longus, and soleus muscles mounted in optimal cutting  
679 temperature compound and frozen in liquid nitrogen-cooled isopentane using a Leica

680 3050S cryotome. Muscle sections were fixed with 4% paraformaldehyde in PBS for five  
681 minutes at room temperature followed by ten minutes of permeabilization using 0.25%  
682 (v/v) Triton X-100 in PBS. Next, sections were washed with PBS three times for 2-minutes  
683 each wash. Sections were blocked for one-hour at room temperature with blocking buffer  
684 (PBS supplemented with 5% goat serum and 1% BSA). Sections were incubated  
685 overnight at 4°C with a primary antibody against laminin (1:100 dilution, Millipore Sigma;  
686 Cat. No. L9393) to label myofiber membranes. Following four PBS washes, sections were  
687 incubated for one-hour with Alexa-Fluor secondary antibodies (ThermoFisher Scientific,  
688 1:100 dilution), and then was four times (five minutes each) and coverslips were mounted  
689 with Vectashield hardmount containing DAPI (Vector Laboratories; Cat. No. H1500) to  
690 label nuclei. Muscle sections were imaged at 20x magnification using an Evos FL2 Auto  
691 microscope. All images were analyzed for CSA using MuscleJ (105).

692

693 **ATAC Sequencing.** Nuclei were isolated by gentle homogenization (10 mM Tris-HCl (pH  
694 7.5), 10 mM NaCl, 3 mM MgCl<sub>2</sub>, 0.1% Tween-20, 0.1% NP-40, and 0.01% Digitonin) of  
695 skeletal muscle followed by tagmentation (Tagment DNA buffer and Tn5, Illumina) for 30  
696 minutes at 37°C. DNA was then purified with the MinElute purification kit from Qiagen. The  
697 purified DNA was PCR amplified for 15 cycles using Q5 High Fidelity DNA polymerase  
698 (New England Biolabs, M0491S) with the incorporation of Illumina Nextera XT adaptors  
699 (Illumina). The libraries were then size selected with AmpureXP Beads (Beckman, Cat#  
700 A63880). Quality control of the libraries was verified using a bioanalyzer. Libraries were  
701 sequenced on Illumina HiSeq4000 using Paired End (PE) 150 bp. The reads were first  
702 mapped to the GRCm39-mm39 mouse genome assembly using Bowtie2 version 2.1.0.

703 Mitochondrial, duplicate, and non-unique reads were removed before peak calling.  
704 MACS2 was used for peak calling employing BAMPE mode. Differentially expressed  
705 peaks were identified using edgeR.

706

707 **Statistical Analysis.** Data are presented as the mean  $\pm$  SD. Normality of data was  
708 assessed using the Shapiro-Wilk test. Data without normal distribution were analyzed  
709 using a Kruskal-Wallis test. Data involving comparisons of two groups were analyzed  
710 using a two-tailed Student's *t*-test. Data involving comparisons of more than two groups  
711 were analyzed using either a one-way ANOVA with Tukey's post hoc or a two-way  
712 ANOVA with Dunnett's post hoc testing for multiple comparisons when significant  
713 interactions were detected. Pearson correlations involved two-tailed statistical testing. All  
714 analyses were performed in GraphPad Prism (Version 9.5.1).  $P < 0.05$  was considered  
715 significant.

716

717 **Study Approval.** All human experiments in this study were approved by the institutional  
718 review boards (Protocol IRB201801553) at the University of Florida and the Malcom  
719 Randall VA Medical Center (Gainesville, FL). All animal experiments in this study were  
720 approved by the Institutional Animal Care and Use Committee of the University of Florida  
721 (Protocol 202110484).

722

723 **Data Availability.** A single XLS file that provides all data in the manuscript and  
724 supplement has been made available with this publication. Raw sequencing data have  
725 been uploaded to the Gene Expression Omnibus (Accession Number GSE255812).

726

727 **Acknowledgements:** This study was supported by National Institutes of Health (NIH)  
728 grant R01-HL149704 (T.E.R.). S.T.S was supported by NIH grant R01HL148597. T.T.  
729 was support by NIH grant F31-DK128920. K.W. was supported by NIH grant T32-  
730 AG062728.

731

732 **Author Contributions:** TT and TER designed the study; TT, NAV, LES, KW, STS, and  
733 TER conducted experiments. TT, NAV, LES, KW, and TER analyzed data. TT, NAV, LES,  
734 KW, STS, and TER interpreted the data. TT and TER drafted the manuscript. TT, NAV,  
735 LES, KW, STS, and TER edited and revised the manuscript. All authors approved the  
736 final version of this manuscript.

737

## 738 **CITATIONS**

- 739 1. Collaborators GBoDS. Global, regional, and national incidence, prevalence, and years lived  
740 with disability for 301 acute and chronic diseases and injuries in 188 countries, 1990-  
741 2013: a systematic analysis for the Global Burden of Disease Study 2013. *Lancet*.  
742 2015;386(9995):743-800.
- 743 2. Gamboa JL, Roshanravan B, Towse T, Keller CA, Falck AM, Yu C, et al. Skeletal Muscle  
744 Mitochondrial Dysfunction Is Present in Patients with CKD before Initiation of  
745 Maintenance Hemodialysis. *Clin J Am Soc Nephrol*. 2020;15(7):926-36.
- 746 3. Gregg LP, Bossola M, Ostrosky-Frid M, and Hedayati SS. Fatigue in CKD: Epidemiology,  
747 Pathophysiology, and Treatment. *Clin J Am Soc Nephrol*. 2021;16(9):1445-55.
- 748 4. Kestenbaum B, Gamboa J, Liu S, Ali AS, Shankland E, Jue T, et al. Impaired skeletal muscle  
749 mitochondrial bioenergetics and physical performance in chronic kidney disease. *JCI*  
750 *Insight*. 2020;5(5).
- 751 5. Mori K. Maintenance of Skeletal Muscle to Counteract Sarcopenia in Patients with  
752 Advanced Chronic Kidney Disease and Especially Those Undergoing Hemodialysis.  
753 *Nutrients*. 2021;13(5).
- 754 6. Wang XH, Du J, Klein JD, Bailey JL, and Mitch WE. Exercise ameliorates chronic kidney  
755 disease-induced defects in muscle protein metabolism and progenitor cell function.  
756 *Kidney Int*. 2009;76(7):751-9.

- 757 7. Wang X, Hu Z, Hu J, Du J, and Mitch WE. Insulin resistance accelerates muscle protein  
758 degradation: Activation of the ubiquitin-proteasome pathway by defects in muscle cell  
759 signaling. *Endocrinology*. 2006;147(9):4160-8.
- 760 8. Mitch WE. Malnutrition is an unusual cause of decreased muscle mass in chronic kidney  
761 disease. *J Ren Nutr*. 2007;17(1):66-9.
- 762 9. May RC, Kelly RA, and Mitch WE. Mechanisms for defects in muscle protein metabolism  
763 in rats with chronic uremia. Influence of metabolic acidosis. *J Clin Invest*. 1987;79(4):1099-  
764 103.
- 765 10. Wang XH, and Mitch WE. Mechanisms of muscle wasting in chronic kidney disease. *Nat*  
766 *Rev Nephrol*. 2014;10(9):504-16.
- 767 11. Thomas SS, and Mitch WE. Mechanisms stimulating muscle wasting in chronic kidney  
768 disease: the roles of the ubiquitin-proteasome system and myostatin. *Clin Exp Nephrol*.  
769 2013;17(2):174-82.
- 770 12. Wang XH, and Mitch WE. Muscle wasting from kidney failure-a model for catabolic  
771 conditions. *Int J Biochem Cell Biol*. 2013;45(10):2230-8.
- 772 13. Price SR, Bailey JL, Wang X, Jurkovitz C, England BK, Ding X, et al. Muscle wasting in  
773 insulinopenic rats results from activation of the ATP-dependent, ubiquitin-proteasome  
774 proteolytic pathway by a mechanism including gene transcription. *J Clin Invest*.  
775 1996;98(8):1703-8.
- 776 14. Zhang L, Rajan V, Lin E, Hu Z, Han HQ, Zhou X, et al. Pharmacological inhibition of  
777 myostatin suppresses systemic inflammation and muscle atrophy in mice with chronic  
778 kidney disease. *FASEB J*. 2011;25(5):1653-63.
- 779 15. Mitch WE. Proteolytic mechanisms, not malnutrition, cause loss of muscle mass in kidney  
780 failure. *J Ren Nutr*. 2006;16(3):208-11.
- 781 16. Durozard D, Pimmel P, Baretto S, Caillette A, Labeeuw M, Baverel G, et al. 31P NMR  
782 spectroscopy investigation of muscle metabolism in hemodialysis patients. *Kidney Int*.  
783 1993;43(4):885-92.
- 784 17. Thompson CH, Kemp GJ, Taylor DJ, Ledingham JG, Radda GK, and Rajagopalan B. Effect of  
785 chronic uraemia on skeletal muscle metabolism in man. *Nephrol Dial Transplant*.  
786 1993;8(3):218-22.
- 787 18. Roshanravan B, Kestenbaum B, Gamboa J, Jubrias SA, Ayers E, Curtin L, et al. CKD and  
788 Muscle Mitochondrial Energetics. *Am J Kidney Dis*. 2016;68(4):658-9.
- 789 19. Roshanravan B, Gamboa J, and Wilund K. Exercise and CKD: Skeletal Muscle Dysfunction  
790 and Practical Application of Exercise to Prevent and Treat Physical Impairments in CKD.  
791 *Am J Kidney Dis*. 2017;69(6):837-52.
- 792 20. Gamboa JL, Billings FT, Bojanowski MT, Gilliam LA, Yu C, Roshanravan B, et al.  
793 Mitochondrial dysfunction and oxidative stress in patients with chronic kidney disease.  
794 *Physiol Rep*. 2016;4(9).
- 795 21. Chalupsky M, Goodson DA, Gamboa JL, and Roshanravan B. New insights into muscle  
796 function in chronic kidney disease and metabolic acidosis. *Curr Opin Nephrol Hypertens*.  
797 2021;30(3):369-76.
- 798 22. Thome T, Kumar RA, Burke SK, Khattri RB, Salyers ZR, Kelley RC, et al. Impaired muscle  
799 mitochondrial energetics is associated with uremic metabolite accumulation in chronic  
800 kidney disease. *Jci Insight*. 2021;6(1).

- 801 23. Thome T, Coleman MD, and Ryan TE. Mitochondrial Bioenergetic and Proteomic  
802 Phenotyping Reveals Organ-Specific Consequences of Chronic Kidney Disease in Mice.  
803 *Cells*. 2021;10(12).
- 804 24. Kim K, Anderson EM, Thome T, Lu GY, Salyers ZR, Cort TA, et al. Skeletal myopathy in CKD:  
805 a comparison of adenine-induced nephropathy and 5/6 nephrectomy models in mice. *Am*  
806 *J Physiol-Renal*. 2021;321(1):F106-F19.
- 807 25. Thome T, Salyers ZR, Kumar RA, Hahn D, Berru FN, Ferreira LF, et al. Uremic metabolites  
808 impair skeletal muscle mitochondrial energetics through disruption of the electron  
809 transport system and matrix dehydrogenase activity. *Am J Physiol Cell Physiol*.  
810 2019;317(4):C701-C13.
- 811 26. Enoki Y, Watanabe H, Arake R, Sugimoto R, Imafuku T, Tominaga Y, et al. Indoxyl sulfate  
812 potentiates skeletal muscle atrophy by inducing the oxidative stress-mediated expression  
813 of myostatin and atrogin-1. *Sci Rep*. 2016;6:32084.
- 814 27. Enoki Y, Watanabe H, Arake R, Fujimura R, Ishiodori K, Imafuku T, et al. Potential  
815 therapeutic interventions for chronic kidney disease-associated sarcopenia via indoxyl  
816 sulfate-induced mitochondrial dysfunction. *J Cachexia Sarcopenia Muscle*. 2017;8(5):735-  
817 47.
- 818 28. Yazdi PG, Moradi H, Yang JY, Wang PH, and Vaziri ND. Skeletal muscle mitochondrial  
819 depletion and dysfunction in chronic kidney disease. *Int J Clin Exp Med*. 2013;6(7):532-9.
- 820 29. Graboski AL, and Redinbo MR. Gut-Derived Protein-Bound Uremic Toxins. *Toxins (Basel)*.  
821 2020;12(9).
- 822 30. Jourde-Chiche N, and Burtey S. Accumulation of protein-bound uremic toxins: the kidney  
823 remains the leading culprit in the gut-liver-kidney axis. *Kidney Int*. 2020;97(6):1102-4.
- 824 31. Vanholder R, De Smet R, Glorieux G, Argilés A, Baurmeister U, Brunet P, et al. Review on  
825 uremic toxins: classification, concentration, and interindividual variability. *Kidney Int*.  
826 2003;63(5):1934-43.
- 827 32. Iitaka M, Kawasaki S, Sakurai S, Hara Y, Kuriyama R, Yamanaka K, et al. Serum substances  
828 that interfere with thyroid hormone assays in patients with chronic renal failure. *Clin*  
829 *Endocrinol (Oxf)*. 1998;48(6):739-46.
- 830 33. Sato E, Mori T, Mishima E, Suzuki A, Sugawara S, Kurasawa N, et al. Metabolic alterations  
831 by indoxyl sulfate in skeletal muscle induce uremic sarcopenia in chronic kidney disease.  
832 *Sci Rep*. 2016;6:36618.
- 833 34. Jang IY, Park JH, Kim JH, Lee S, Lee E, Lee JY, et al. The association of circulating  
834 kynurenine, a tryptophan metabolite, with frailty in older adults. *Aging-US*.  
835 2020;12(21):22253-65.
- 836 35. Westbrook R, Chung T, Lovett J, Ward C, Joca H, Yang HL, et al. Kynurenines link chronic  
837 inflammation to functional decline and physical frailty. *Jci Insight*. 2020;5(16).
- 838 36. Saito K, Fujigaki S, Heyes MP, Shibata K, Takemura M, Fujii H, et al. Mechanism of  
839 increases in L-kynurenine and quinolinic acid in renal insufficiency. *Am J Physiol Renal*  
840 *Physiol*. 2000;279(3):F565-72.
- 841 37. Schroeder JC, Dinatale BC, Murray IA, Flaveny CA, Liu Q, Laurenzana EM, et al. The uremic  
842 toxin 3-indoxyl sulfate is a potent endogenous agonist for the human aryl hydrocarbon  
843 receptor. *Biochemistry*. 2010;49(2):393-400.

- 844 38. Denison MS, and Nagy SR. Activation of the aryl hydrocarbon receptor by structurally  
845 diverse exogenous and endogenous chemicals. *Annu Rev Pharmacol Toxicol.*  
846 2003;43:309-34.
- 847 39. Rothhammer V, and Quintana FJ. The aryl hydrocarbon receptor: an environmental  
848 sensor integrating immune responses in health and disease. *Nat Rev Immunol.*  
849 2019;19(3):184-97.
- 850 40. Avilla MN, Malecki KMC, Hahn ME, Wilson RH, and Bradfield CA. The Ah Receptor:  
851 Adaptive Metabolism, Ligand Diversity, and the Xenokine Model. *Chem Res Toxicol.*  
852 2020;33(4):860-79.
- 853 41. Stevens EA, Mezrich JD, and Bradfield CA. The aryl hydrocarbon receptor: a perspective  
854 on potential roles in the immune system. *Immunology.* 2009;127(3):299-311.
- 855 42. Sato S, Shirakawa H, Tomita S, Ohsaki Y, Haketa K, Tooi O, et al. Low-dose dioxins alter  
856 gene expression related to cholesterol biosynthesis, lipogenesis, and glucose metabolism  
857 through the aryl hydrocarbon receptor-mediated pathway in mouse liver. *Toxicol Appl*  
858 *Pharmacol.* 2008;229(1):10-9.
- 859 43. Lee JH, Wada T, Febbraio M, He J, Matsubara T, Lee MJ, et al. A novel role for the dioxin  
860 receptor in fatty acid metabolism and hepatic steatosis. *Gastroenterology.*  
861 2010;139(2):653-63.
- 862 44. Wang C, Xu CX, Krager SL, Bottum KM, Liao DF, and Tischkau SA. Aryl hydrocarbon  
863 receptor deficiency enhances insulin sensitivity and reduces PPAR- $\alpha$  pathway activity in  
864 mice. *Environ Health Perspect.* 2011;119(12):1739-44.
- 865 45. Warner M, Mocarelli P, Brambilla P, Wesselink A, Samuels S, Signorini S, et al. Diabetes,  
866 metabolic syndrome, and obesity in relation to serum dioxin concentrations: the Seveso  
867 women's health study. *Environ Health Perspect.* 2013;121(8):906-11.
- 868 46. Dou L, Poitevin S, Sallee M, Addi T, Gondouin B, McKay N, et al. Aryl hydrocarbon receptor  
869 is activated in patients and mice with chronic kidney disease. *Kidney Int.* 2018;93(4):986-  
870 99.
- 871 47. Walker JA, Richards S, Belghasem ME, Arinze N, Yoo SB, Tashjian JY, et al. Temporal and  
872 tissue-specific activation of aryl hydrocarbon receptor in discrete mouse models of kidney  
873 disease. *Kidney Int.* 2020;97(3):538-50.
- 874 48. Thome T, Miguez K, Willms AJ, Burke SK, Chandran V, de Souza AR, et al. Chronic aryl  
875 hydrocarbon receptor activity phenocopies smoking-induced skeletal muscle impairment.  
876 *J Cachexia Sarcopenia Muscle.* 2022;13(1):589-604.
- 877 49. Balestrieri N, Palzkill V, Pass C, Tan J, Salyers ZR, Moparthy C, et al. Activation of the Aryl  
878 Hydrocarbon Receptor in Muscle Exacerbates Ischemic Pathology in Chronic Kidney  
879 Disease. *Circulation research.* 2023;133(2):158-76.
- 880 50. Durantou F, Cohen G, De Smet R, Rodriguez M, Jankowski J, Vanholder R, et al. Normal  
881 and pathologic concentrations of uremic toxins. *J Am Soc Nephrol.* 2012;23(7):1258-70.
- 882 51. Vanholder R, Schepers E, Pletinck A, Neiryneck N, and Glorieux G. An update on protein-  
883 bound uremic retention solutes. *J Ren Nutr.* 2012;22(1):90-4.
- 884 52. Swan JS, Kragten EY, and Veening H. Liquid-chromatographic study of fluorescent  
885 materials in uremic fluids. *Clin Chem.* 1983;29(6):1082-4.
- 886 53. Niwa T, and Ise M. Indoxyl sulfate, a circulating uremic toxin, stimulates the progression  
887 of glomerular sclerosis. *J Lab Clin Med.* 1994;124(1):96-104.

- 888 54. Bush KT, Singh P, and Nigam SK. Gut-derived uremic toxin handling in vivo requires OAT-  
889 mediated tubular secretion in chronic kidney disease. *Jci Insight*. 2020;5(7).
- 890 55. Palzkill VR, Thome T, Murillo AL, Khattri RB, and Ryan TE. Increasing plasma L-kynurenine  
891 impairs mitochondrial oxidative phosphorylation prior to the development of atrophy in  
892 murine skeletal muscle: A pilot study. *Frontiers in physiology*. 2022;13.
- 893 56. Wilson RH, and Bradfield CA. Rodent genetic models of Ah receptor signaling. *Drug Metab*  
894 *Rev*. 2021;53(3):350-74.
- 895 57. Niwa A, Kumaki K, Nebert DW, and Poland AP. Genetic expression of aryl hydrocarbon  
896 hydroxylase activity in the mouse. Distinction between the "responsive" homozygote and  
897 heterozygote at the Ah locus. *Arch Biochem Biophys*. 1975;166(2):559-64.
- 898 58. Poland A, Glover E, and Kende AS. Stereospecific, high affinity binding of 2,3,7,8-  
899 tetrachlorodibenzo-p-dioxin by hepatic cytosol. Evidence that the binding species is  
900 receptor for induction of aryl hydrocarbon hydroxylase. *J Biol Chem*. 1976;251(16):4936-  
901 46.
- 902 59. Tabebordbar M, Lagerborg KA, Stanton A, King EM, Ye S, Tellez L, et al. Directed evolution  
903 of a family of AAV capsid variants enabling potent muscle-directed gene delivery across  
904 species. *Cell*. 2021;184(19):4919-38.e22.
- 905 60. Andersson P, McGuire J, Rubio C, Gradin K, Whitelaw ML, Pettersson S, et al. A  
906 constitutively active dioxin/aryl hydrocarbon receptor induces stomach tumors. *Proc Natl*  
907 *Acad Sci U S A*. 2002;99(15):9990-5.
- 908 61. Seok SH, Lee W, Jiang L, Molugu K, Zheng A, Li Y, et al. Structural hierarchy controlling  
909 dimerization and target DNA recognition in the AHR transcriptional complex. *Proc Natl*  
910 *Acad Sci U S A*. 2017;114(21):5431-6.
- 911 62. Wang XH, Mitch WE, and Price SR. Pathophysiological mechanisms leading to muscle loss  
912 in chronic kidney disease. *Nat Rev Nephrol*. 2022;18(3):138-52.
- 913 63. Watson EL, Baker LA, Wilkinson TJ, Gould DW, Graham-Brown MPM, Major RW, et al.  
914 Reductions in skeletal muscle mitochondrial mass are not restored following exercise  
915 training in patients with chronic kidney disease. *Faseb J*. 2020;34(1):1755-67.
- 916 64. Thome T, Kim K, Dong G, and Ryan TE. The Role of Mitochondrial and Redox Alterations  
917 in the Skeletal Myopathy Associated with Chronic Kidney Disease. *Antioxidants & redox*  
918 *signaling*. 2023;38(4-6):318-37.
- 919 65. Barreto FC, Barreto DV, Liabeuf S, Meert N, Glorieux G, Temmar M, et al. Serum indoxyl  
920 sulfate is associated with vascular disease and mortality in chronic kidney disease  
921 patients. *Clin J Am Soc Nephrol*. 2009;4(10):1551-8.
- 922 66. Schefold JC, Zeden JP, Fotopoulou C, von Haehling S, Pschowski R, Hasper D, et al.  
923 Increased indoleamine 2,3-dioxygenase (IDO) activity and elevated serum levels of  
924 tryptophan catabolites in patients with chronic kidney disease: a possible link between  
925 chronic inflammation and uraemic symptoms. *Nephrol Dial Transplant*. 2009;24(6):1901-  
926 8.
- 927 67. Cheng Y, Li Y, Benkowitz P, Lamina C, Köttgen A, and Sekula P. The relationship between  
928 blood metabolites of the tryptophan pathway and kidney function: a bidirectional  
929 Mendelian randomization analysis. *Sci Rep*. 2020;10(1):12675.

- 930 68. Bao YS, Ji Y, Zhao SL, Ma LL, Xie RJ, and Na SP. Serum levels and activity of indoleamine2,3-  
931 dioxygenase and tryptophanyl-tRNA synthetase and their association with disease  
932 severity in patients with chronic kidney disease. *Biomarkers*. 2013;18(5):379-85.
- 933 69. Niwa T, Yazawa T, Ise M, Sugano M, Kodama T, Uehara Y, et al. Inhibitory effect of oral  
934 sorbent on accumulation of albumin-bound indoxyl sulfate in serum of experimental  
935 uremic rats. *Nephron*. 1991;57(1):84-8.
- 936 70. Nishikawa M, Ishimori N, Takada S, Saito A, Kadoguchi T, Furihata T, et al. AST-120  
937 ameliorates lowered exercise capacity and mitochondrial biogenesis in the skeletal  
938 muscle from mice with chronic kidney disease via reducing oxidative stress. *Nephrol Dial  
939 Transplant*. 2015;30(6):934-42.
- 940 71. Cha RH, Kang SH, Han MY, An WS, Kim SH, and Kim JC. Effects of AST-120 on muscle health  
941 and quality of life in chronic kidney disease patients: results of RECOVERY study. *J  
942 Cachexia Sarcopenia Muscle*. 2022;13(1):397-408.
- 943 72. Kou Z, and Dai W. Aryl hydrocarbon receptor: Its roles in physiology. *Biochem Pharmacol*.  
944 2021;185:114428.
- 945 73. Anderson G, Beischlag TV, Vinciguerra M, and Mazzoccoli G. The circadian clock circuitry  
946 and the AHR signaling pathway in physiology and pathology. *Biochem Pharmacol*.  
947 2013;85(10):1405-16.
- 948 74. Dalton TP, Kerzee JK, Wang B, Miller M, Dieter MZ, Lorenz JN, et al. Dioxin exposure is an  
949 environmental risk factor for ischemic heart disease. *Cardiovasc Toxicol*. 2001;1(4):285-  
950 98.
- 951 75. Bock KW. Functions of aryl hydrocarbon receptor (AHR) and CD38 in NAD metabolism and  
952 nonalcoholic steatohepatitis (NASH). *Biochem Pharmacol*. 2019;169:113620.
- 953 76. Ghosh J, Chowdhury AR, Srinivasan S, Chattopadhyay M, Bose M, Bhattacharya S, et al.  
954 Cigarette Smoke Toxins-Induced Mitochondrial Dysfunction and Pancreatitis Involves Aryl  
955 Hydrocarbon Receptor Mediated Cyp1 Gene Expression: Protective Effects of Resveratrol.  
956 *Toxicol Sci*. 2018;166(2):428-40.
- 957 77. Huang Y, Zhang J, Tao Y, Ji C, Anigu S, Jiang Y, et al. AHR/ROS-mediated mitochondria  
958 apoptosis contributes to benzo[a]pyrene-induced heart defects and the protective effects  
959 of resveratrol. *Toxicology*. 2021;462:152965.
- 960 78. Heo MJ, Suh JH, Lee SH, Poulsen KL, An YA, Moorthy B, et al. Aryl hydrocarbon receptor  
961 maintains hepatic mitochondrial homeostasis in mice. *Mol Metab*. 2023;72:101717.
- 962 79. Kolachalama VB, Shashar M, Alousi F, Shivanna S, Rijal K, Belghasem ME, et al. Uremic  
963 Solute-Aryl Hydrocarbon Receptor-Tissue Factor Axis Associates with Thrombosis after  
964 Vascular Injury in Humans. *Journal of the American Society of Nephrology*.  
965 2018;29(3):1063-72.
- 966 80. Wilson RH, Carney PR, Glover E, Parrott JC, Rojas BL, Moran SM, et al. Generation of an  
967 Allelic Series at the Ahr Locus Using an Edited Recombinant Approach. *Toxicological  
968 Sciences*. 2021;180(2):239-51.
- 969 81. Bittel DC, Bittel AJ, Varadhachary AS, Pietka T, and Sinacore DR. Deficits in the Skeletal  
970 Muscle Transcriptome and Mitochondrial Coupling in Progressive Diabetes-Induced CKD  
971 Relate to Functional Decline. *Diabetes*. 2021;70(5):1130-44.

972 82. Gamboa JL, Roshanravan B, Towse T, Keller CA, Falck AM, Yu C, et al. Skeletal Muscle  
973 Mitochondrial Dysfunction Is Present in Patients with CKD before Initiation of  
974 Maintenance Hemodialysis. *Clin J Am Soc Nephro*. 2020;15(7):926-36.

975 83. Lee J, Prokopec SD, Watson JD, Sun RX, Pohjanvirta R, and Boutros PC. Male and female  
976 mice show significant differences in hepatic transcriptomic response to 2,3,7,8-  
977 tetrachlorodibenzo-p-dioxin. *BMC Genomics*. 2015;16(1):625.

978 84. Ohtake F, Baba A, Fujii-Kuriyama Y, and Kato S. Intrinsic AhR function underlies cross-talk  
979 of dioxins with sex hormone signalings. *Biochem Biophys Res Commun*. 2008;370(4):541-  
980 6.

981 85. Ohtake F, Baba A, Takada I, Okada M, Iwasaki K, Miki H, et al. Dioxin receptor is a ligand-  
982 dependent E3 ubiquitin ligase. *Nature*. 2007;446(7135):562-6.

983 86. Karman BN, Basavarajappa MS, Craig ZR, and Flaws JA. 2,3,7,8-Tetrachlorodibenzo-p-  
984 dioxin activates the aryl hydrocarbon receptor and alters sex steroid hormone secretion  
985 without affecting growth of mouse antral follicles in vitro. *Toxicol Appl Pharmacol*.  
986 2012;261(1):88-96.

987 87. Serrano E, Whitaker-Menezes D, Lin Z, Roche M, and Martinez Cantarin MP. Uremic  
988 Myopathy and Mitochondrial Dysfunction in Kidney Disease. *Int J Mol Sci*. 2022;23(21).

989 88. Xu C, Kasimumali A, Guo X, Lu R, Xie K, Zhu M, et al. Reduction of mitochondria and up  
990 regulation of pyruvate dehydrogenase kinase 4 of skeletal muscle in patients with chronic  
991 kidney disease. *Nephrology (Carlton)*. 2020;25(3):230-8.

992 89. Dodd SL, Gagnon BJ, Senf SM, Hain BA, and Judge AR. ROS-Mediated Activation of NF-  
993 kappa B and FOXO Dduring Muscle Disuse. *Muscle Nerve*. 2010;41(1):110-3.

994 90. Powers SK, Morton AB, Ahn B, and Smuder AJ. Redox control of skeletal muscle atrophy.  
995 *Free Radical Bio Med*. 2016;98:208-17.

996 91. Vellanki K, and Hou S. Menopause in CKD. *Am J Kidney Dis*. 2018;71(5):710-9.

997 92. Bailey JL, Zheng B, Hu Z, Price SR, and Mitch WE. Chronic kidney disease causes defects in  
998 signaling through the insulin receptor substrate/phosphatidylinositol 3-kinase/Akt  
999 pathway: implications for muscle atrophy. *Journal of the American Society of Nephrology*  
1000 : *JASN*. 2006;17(5):1388-94.

1001 93. Zhang L, Wang XH, Wang H, Du J, and Mitch WE. Satellite cell dysfunction and impaired  
1002 IGF-1 signaling cause CKD-induced muscle atrophy. *Journal of the American Society of*  
1003 *Nephrology : JASN*. 2010;21(3):419-27.

1004 94. Diwan V, Mistry A, Gobe G, and Brown L. Adenine-induced chronic kidney and  
1005 cardiovascular damage in rats. *J Pharmacol Toxicol Methods*. 2013;68(2):197-207.

1006 95. Xia X, Luo Q, Li B, Lin Z, Yu X, and Huang F. Serum uric acid and mortality in chronic kidney  
1007 disease: A systematic review and meta-analysis. *Metabolism*. 2016;65(9):1326-41.

1008 96. Miller SG, Matias C, Hafen PS, Law AS, Witczak CA, and Brault JJ. Uric acid formation is  
1009 driven by crosstalk between skeletal muscle and other cell types. *JCI Insight*. 2023.

1010 97. Ryan TE, Kim K, Scali ST, Berceci SA, Thome T, Salyers ZR, et al. Interventional- and  
1011 amputation-stage muscle proteomes in the chronically threatened ischemic limb. *Clinical*  
1012 *and Translational Medicine*. 2022;12(1):e658.

1013 98. Inker LA, Eneanya ND, Coresh J, Tighiouart H, Wang D, Sang YY, et al. New Creatinine- and  
1014 Cystatin C-Based Equations to Estimate GFR without Race. *New Engl J Med*.  
1015 2021;385(19):1737-49.

1016 99. Thome T, Miguez K, Willms A, Burke SK, Chandran V, de Souza AR, et al. Chronic aryl  
1017 hydrocarbon receptor activity phenocopies smoking-induced skeletal muscle impairment.  
1018 *J Cachexia Sarcopeni*. 2021.  
1019 100. Ryan TE, Yamaguchi DJ, Schmidt CA, Zeczycki TN, Shaikh SR, Brophy P, et al. Extensive  
1020 skeletal muscle cell mitochondriopathy distinguishes critical limb ischemia patients from  
1021 claudicants. *JCI Insight*. 2018;3(21).  
1022 101. Tabebordbar M, Lagerborg KA, Stanton A, King EM, Ye S, Tellez L, et al. Directed evolution  
1023 of a family of AAV capsid variants enabling potent muscle-directed gene delivery across  
1024 species. *Cell*. 2021;184(19):4919-+.  
1025 102. Qi Z, Whitt I, Mehta A, Jin J, Zhao M, Harris RC, et al. Serial determination of glomerular  
1026 filtration rate in conscious mice using FITC-inulin clearance. *American journal of*  
1027 *physiology Renal physiology*. 2004;286(3):F590-6.  
1028 103. Rieg T. A High-throughput method for measurement of glomerular filtration rate in  
1029 conscious mice. *J Vis Exp*. 2013(75):e50330.  
1030 104. Fisher-Wellman KH, Davidson MT, Narowski TM, Lin CT, Koves TR, and Muoio DM.  
1031 Mitochondrial Diagnostics: A Multiplexed Assay Platform for Comprehensive Assessment  
1032 of Mitochondrial Energy Fluxes. *Cell reports*. 2018;24(13):3593-606 e10.  
1033 105. Mayeuf-Louchart A, Hardy D, Thorel Q, Roux P, Gueniot L, Briand D, et al. MuscleJ: a high-  
1034 content analysis method to study skeletal muscle with a new Fiji tool. *Skelet Muscle*.  
1035 2018;8(1):25.  
1036

1037

1038

1039

1040

1041

1042

1043

1044

1045

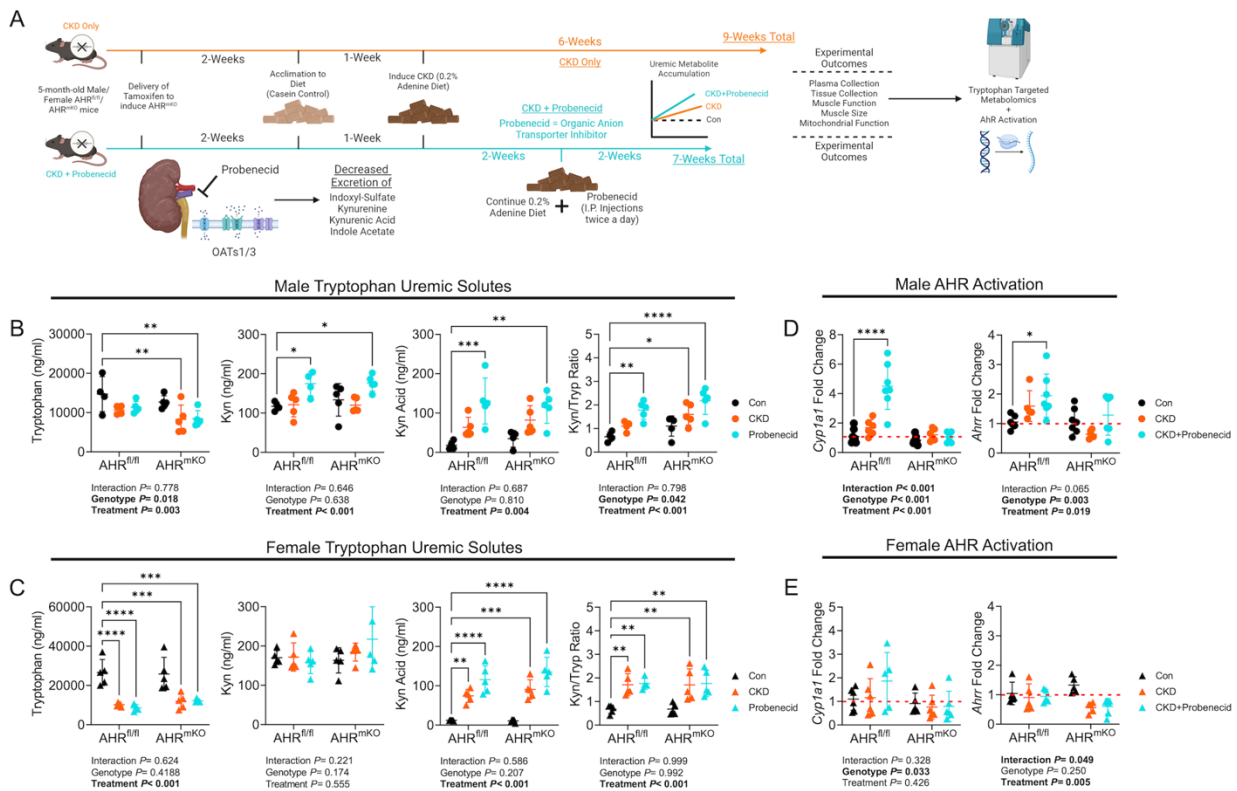
1046

1047

1048



1063  
1064



1065

1066

1067

1068

1069

1070

1071

1072

1073

1074

1075

1076

1077

1078

1079

1080

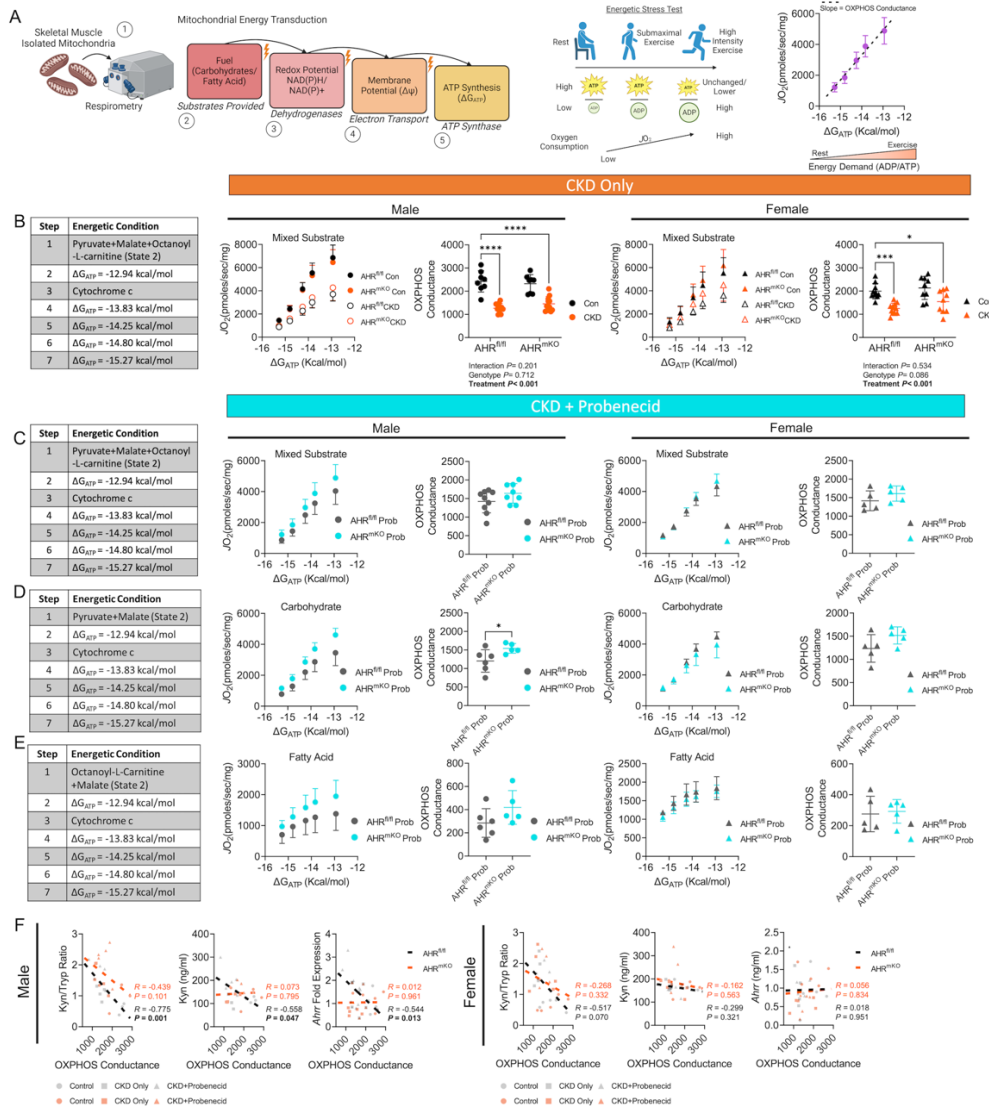
1081

1082

1083

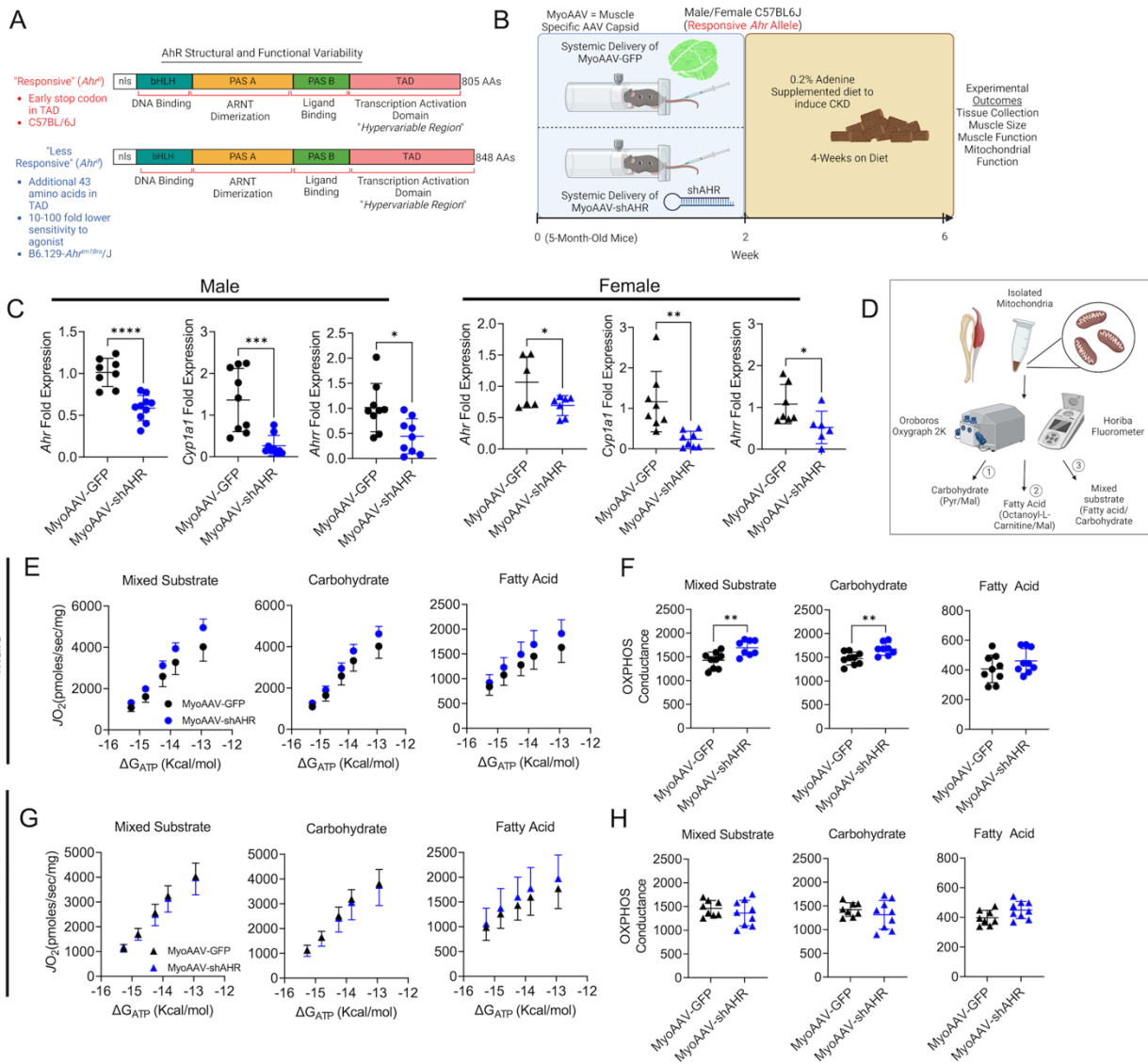
1084

**Figure 2. Uremic metabolites accumulation drives AHR activation in CKD muscle which is abolished by muscle specific AHR deletion.** (A) Experimental treatment timeline. (B) Concentrations of tryptophan-derived uremic metabolites in plasma from male  $AHR^{fl/fl}$  and  $AHR^{mKO}$  mice without CKD, with CKD, and with CKD plus daily probenecid treatment ( $n=4-5$ /group/genotype). (C) Concentrations of tryptophan-derived uremic metabolites in plasma from female  $AHR^{fl/fl}$  and  $AHR^{mKO}$  mice without CKD, with CKD, and with CKD plus daily probenecid treatment ( $n=4-5$ /group/genotype). (D) qPCR quantification of *Cyp1a1* and *Ahr* levels in skeletal muscle of male  $AHR^{fl/fl}$  and  $AHR^{mKO}$  mice without CKD, with CKD, and with CKD plus daily probenecid treatment ( $n=5-7$ /group/genotype). (E) qPCR quantification of *Cyp1a1* and *Ahr* levels in skeletal muscle of female  $AHR^{fl/fl}$  and  $AHR^{mKO}$  mice without CKD, with CKD, and with CKD plus daily probenecid treatment ( $n=5-6$ /group/genotype). Statistical analyses performed using two-way ANOVA with Dunnett's post hoc testing for multiple comparisons. Error bars represent standard deviation. \* $P<0.05$ , \*\* $P<0.01$ , \*\*\* $P<0.001$ , \*\*\*\* $P<0.0001$ .



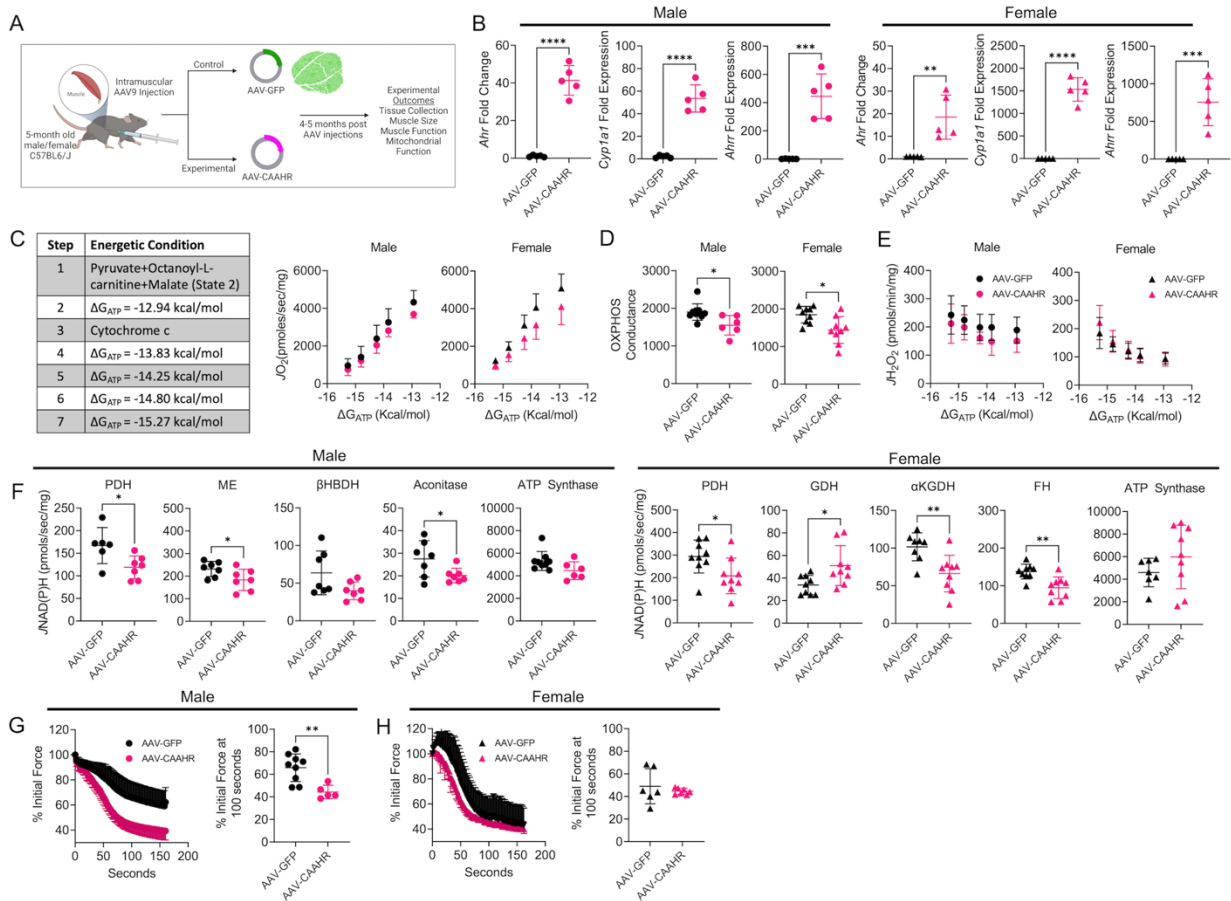
1088 **Figure 3. Muscle specific AHR deletion improves mitochondrial OXPHOS with high**  
 1089 **tryptophan-derive uremic metabolite levels.** (A) Graphical depiction of mitochondrial  
 1090 OXPHOS system and the use of a creatine kinase clamp to measure oxygen consumption  
 1091 ( $JO_2$ ) across physiologically relevant energetic demands ( $\Delta G_{ATP}$ ). (B) Experimental  
 1092 conditions quantification  $JO_2$  at each level of  $\Delta G_{ATP}$ , as well as the OXPHOS conductance  
 1093 in male and female  $AHR^{fl/fl}$  and  $AHR^{mKO}$  mice with or without CKD (n=8-  
 1094 12/group/genotype). Experimental conditions and quantification  $JO_2$  at each level of  
 1095  $\Delta G_{ATP}$ , as well as the OXPHOS conductance in male and female  $AHR^{fl/fl}$  and  $AHR^{mKO}$   
 1096 mice with CKD plus daily probenecid treatment (n=5-9/group/genotype) for mixed  
 1097 substrates (C), pyruvate/malate (D), and octanoylcarnitine/malate (E). (F) Pearson  
 1098 correlational analyses of quantified OXPHOS conductance (mixed substrates) and  
 1099 kynurenine to tryptophan ratio, kynurenine concentrations, and *Ahr* mRNA in male and  
 1100 female  $AHR^{fl/fl}$  and  $AHR^{mKO}$  mice across control, CKD, and CKD plus probenecid daily.

1101 Data were analyzed by two-way ANOVA with Dunnett's post hoc testing for multiple  
 1102 comparisons in panel B. Two-tailed Student's *t*-test were performed in panels C-E. Error  
 1103 bars represent the standard deviation. \**P*<0.05, \*\*\**P*<0.001, \*\*\*\**P*<0.0001.



1104 **Figure 4. Muscle-specific AHR knockdown improves mitochondrial OXPHOS in**  
 1105 **mice harboring the high-affinity AHR allele.** (A) Graphical depiction of polymorphisms  
 1106 in the AHR that confer differences in ligand affinity. (B) Experimental timeline of delivery  
 1107 of MyoAAV-GFP or MyoAAV-shAHR in high-affinity C57BL/6J mice with CKD. (C) qPCR  
 1108 validation of *Ahr* knockdown and subsequent reduction in *Cyp1a1* and *Ahr* mRNA  
 1109 induction in MyoAAV-shAHR mice (n=6-10/group). (D) Graphical depiction of analytical  
 1110 approach for mitochondrial OXPHOS assessments. (E) Relationship between  $JO_2$  and  
 1111  $\Delta G_{ATP}$  in isolated mitochondria from the gastrocnemius muscle in different substrate  
 1112 conditions in male mice with CKD (n=8-9/group). (F) Quantification of OXPHOS  
 1113 conductance in male mice (n=8-9/group). (G) Relationship between  $JO_2$  and  $\Delta G_{ATP}$  in  
 1114 isolated mitochondria from the gastrocnemius muscle in different substrate conditions in  
 1115 female mice with CKD (n=8-9/group). (H) Quantification of OXPHOS conductance in

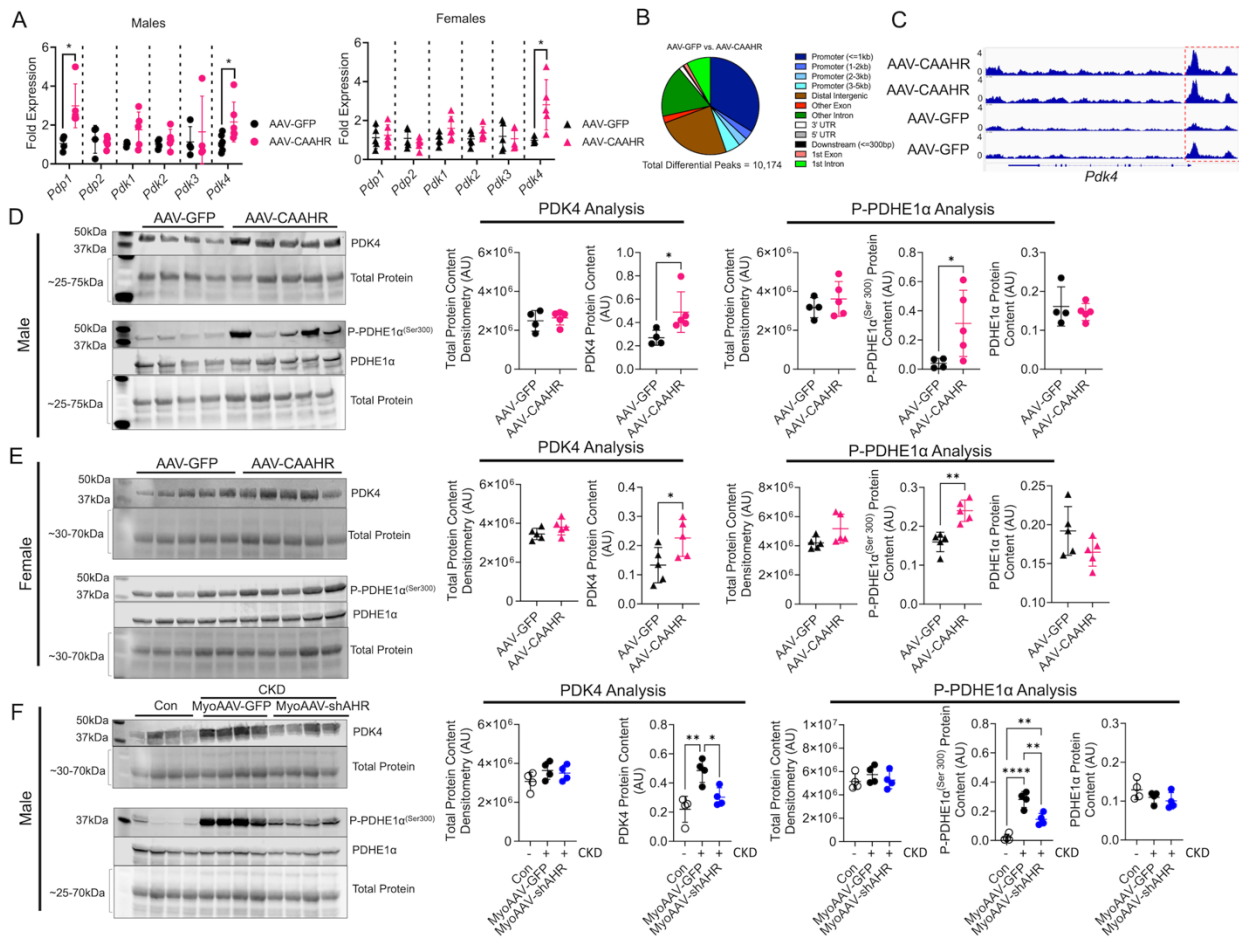
1117 female mice (n=8-9/group). Statistical analyses were performed using two-tailed  
 1118 Student's *t*-test. Error bars represent standard deviation. \**P*<0.05, \*\**P*<0.01, \*\*\**P*<0.001,  
 1119 \*\*\*\**P*<0.0001.



1120  
 1121 **Figure 5. Ectopic expression of a constitutively active AHR impairs muscle**  
 1122 **mitochondrial OXPHOS in mice with normal kidney function.** (A) Experimental design  
 1123 for muscle-specific delivery of mutant constitutively active AHR (CAAHR). (B) qPCR of  
 1124 *Ahr*, *Cyp11a1*, and *Ahrr* in male and female mice treated with AAV-GFP and AAV-CAAHR  
 1125 (n=5/group). (C) Substrate conditions and quantification of the relationship between  $JO_2$   
 1126 and  $\Delta G_{ATP}$  in male and female mice treated with AAV-GFP or AAV-CAAHR (n=6-  
 1127 10/group). (D) OXPHOS conductance in male and female mice (n=6-10/group). (E)  
 1128 Mitochondrial  $JH_2O_2$  and  $\Delta G_{ATP}$  in male and female mice (n=6-10/group). (F)  
 1129 Quantification of mitochondrial matrix dehydrogenase enzyme activity in male and female  
 1130 mice (n=6-9/group). (G) Analysis of extensor digitorum longus muscle fatigue in male and  
 1131 female mice (n=5-9/group). Data analyzed using two-tailed Student's *t*-test. Error bars  
 1132 represent standard deviation. \**P*<0.05, \*\**P*<0.01, \*\*\**P*<0.001, \*\*\*\**P*<0.0001.  
 1133

1134  
 1135  
 1136

1137  
1138

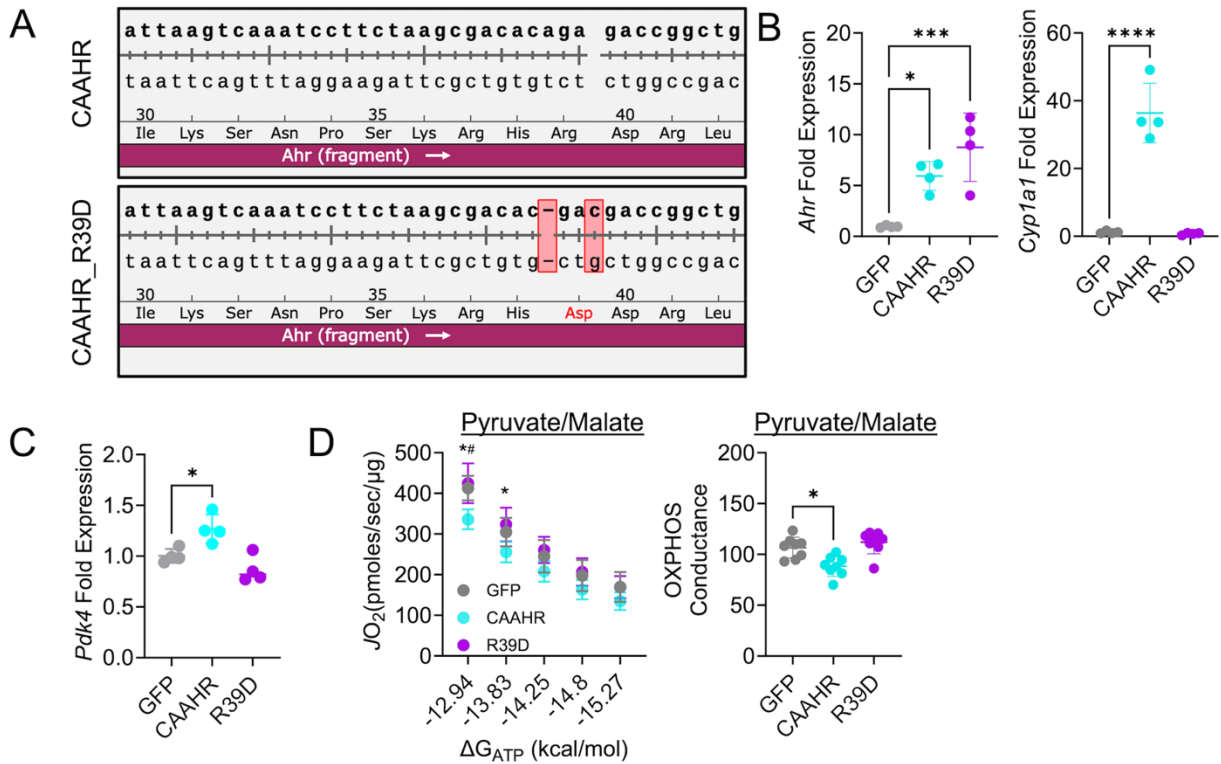


1139

1140 **Figure 6. AHR activation increased PDK4 expression and PDH phosphorylation.** (A)  
1141 qPCR of *Pdp1*, *Pdp2*, *Pdk1*, *Pdk2*, *Pdk3*, and *Pdk4* in male and female mice treated with  
1142 AAV-GFP and AAV-CAAHR (n=5-6/group). (B) Peak annotation pie charts for ATAC-Seq  
1143 peaks in AAV-GFP vs. AAV-CAAHR muscles (n=3/group). (C) IGV snapshots of the *Pdk4*  
1144 gene showing chromatin accessibility with the red-dashed box highlighting the promoter  
1145 region. (D) Western blotting of PDK4, phosphorylated PDHE1α<sup>Ser300</sup>, and total PDHE1α  
1146 protein expression in male AAV-GFP or AAV-CAAHR gastrocnemius muscle (n=4-  
1147 5/group). (E) Western blotting of PDK4, phosphorylated PDHE1α<sup>Ser300</sup>, and total PDHE1α  
1148 protein expression in female AAV-GFP or AAV-CAAHR gastrocnemius muscle  
1149 (n=5/group). (F) Western blotting of PDK4, phosphorylated PDHE1α<sup>Ser300</sup>, and total  
1150 PDHE1α protein expression in male control, CKD MyoAAV-GFP, and CKD MyoAAV-  
1151 shAHR gastrocnemius muscle (n=4/group). Data in panels A, D, and E were analyzed  
1152 using two-tailed Student's *t*-test. Data in Panel F were analyzed using one-way ANOVA  
1153 with Tukey's post-hoc. \**P*<0.05, \*\**P*<0.01, \*\*\*\**P*<0.0001.

1154  
1155  
1156

1157  
1158  
1159



1160  
1161  
1162  
1163  
1164  
1165  
1166  
1167  
1168  
1169  
1170  
1171

**Figure 7. Expression of a transcriptionally inept CAAHR abolishes Pdk4 expression and pyruvate supported OXPHOS impairment in C<sub>2</sub>C<sub>12</sub> muscle cells.** (A) Sequencing results demonstrating the introduction of point mutation that converted arginine-39 to aspartate (R39D). (B) qPCR validation of the overexpression of *Ahr* and lack of transcriptional activity (*Cyp1a1*) in the R39D mutant. A GFP control plasmid was also tested. (n=4/group) (C) *Pdk4* mRNA expression (fold GFP). (n=4/group) (D) Pyruvate supported respiration in muscle cells and quantified OXPHOS conductance. (n=8/group). Error bars represent standard deviation. Data were analyzed using one-way ANOVA with Tukey's post-hoc. \**P*<0.05, \*\**P*<0.01, \*\*\**P*<0.001, \*\*\*\**P*<0.0001. #*P*<0.05 for CAAHR vs. R39D.